Utrecht University

Faculty of Science

From graphene to T-graphene

The electronic and topological properties of one- and two-dimensional square-octagon lattices in a magnetic field

Bachelor Thesis

Salma Ismaili

Physics and Astronomy

Supervisors:

Sander Kempkes MSc

Institute for Theoretical Physics, Utrecht

Prof. Dr. Cristiane Morais Smith

Institute for Theoretical Physics, Utrecht

January 15, 2020

Abstract

The discovery of graphene and its extraordinary properties, which arise from the existence of Dirac cones in the band structure, has sparked interest in other electronic lattices with different geometries. In this thesis, the electronic properties of T-graphene, or a square-octagon lattice, are studied using a tight-binding model. The band structure is calculated for different values of the intracell t_1 and intercell t_2 hopping parameters. A uniaxial strain is introduced and the band structure of the resulting highly anisotropic T-graphene shows the merging of Dirac-like points upon varying the hopping parameters. A finite-size T-graphene system does not show topologically protected edge states due to the hybridization of the zero-energy edge states with the zero-energy excitations in the bulk. To open a gap in the bulk, a magnetic flux is introduced in a T-graphene lattice and the band structures and topological properties are studied. However, no topological phases emerge due to the hybridization of the wave functions of the edge states. Additionally, the band structure of a one-dimensional T-graphene chain is calculated and shows two edge modes at zero energy and no closing of the gap (except for $t_2 = 0$). The calculated Zak phases of the energy bands suggest the absence of topologically protected edge states, but the localization of the wave functions does indicate the existence of robust compact localized states. Further research is needed to determine whether the introduction of superconductivity or Rashba spin-orbit coupling can open the gap to obtain these compact localized states.

Acknowledgements

Writing my Bachelor thesis was the hardest thing I have ever done. Luckily, I have received immense support from my daily supervisor, Sander Kempkes, over the past year. I would like to thank him for all the support and feedback, for taking the time to answer my questions and for reassuring and motivating me when I felt overwhelmed. He proved to be the steady hand that guided me throughout the year. I also want to thank Cristiane Morais Smith for her enthusiasm and infinite supply of ideas. She welcomed me in her group from the start and made me feel like a valued addition. Thanks to them, my first experience with the academic world has been very meaningful.

Furthermore, I would like to thank Peter Jacobse, who was the first to tell us about T-graphene and sparked our interest in this topic, Mikael Fremling, who provided us with a better theoretical understanding of the difference between the types of flux in Chapter 4, and Wouter Beugeling, who read my thesis and confirmed the counter-intuitive results in Chapter 4 and 5.

Contents

Introduction

A new era of two-dimensional materials started with the discovery of graphene. Graphene was first isolated by André Geim and Konstantin Novoselov in 2004 [1]. For years, graphene had been merely a theoretical consideration, and the isolation of a single layer of any material was considered to be impossible. After the isolation, the scientific community was sceptical at first, especially since Geim and Novoselov used the simple Scotch Tape method, in which a piece of tape is used to peel off graphene layers of a piece of graphite. In the following years, the special properties of graphene were discovered and a revolution in condensed matter physics began to unfold. Geim and Novoselov were eventually awarded the Nobel Prize "for groundbreaking experiments regarding the two-dimensional material graphene."

The special properties of graphene arise from the existence of Dirac points, which are points in the band structure where the bands cross linearly. The linear dispersion relation around the Dirac points was originally attributed to the honeycomb structure of graphene. However, Choi *et al.* [2] reported in 2010 that the semimetallic nature of graphene persisted up to a very large uniaxial strain of 30%. This implies that a hexagonal lattice is not a necessary condition for the existence of Dirac fermions. Dirac points were also found to exist in α- and β-graphene [3, 4], 6,14,18-graphyne [5], 6,6,12-graphyne [6] and T-graphene [7]. T-graphene is sometimes also called the square-octagon or diamond-octagon lattice.

In 1988, Haldane introduced a two-dimensional toy model, the Haldane model [8], which uses graphene as a starting point because of its Dirac cones. Haldane showed how to open a gap in the band structure of graphene by introducing complex next-nearest-neighbour (NNN) hopping. As a result, chiral edge states with a topological origin appeared for certain values of the NNN hopping. This Haldane model, or Chern insulator, may be considered the precursor to today's time-reversal invariant topological insulators.

In 2005, Kane and Mele published two papers on the quantum spin Hall (QSH) effect in graphene [9, 10]. They predicted that a band gap could be opened by introducing spin-orbit coupling, but they overestimated the intrinsic spin-orbit coupling of graphene. However, very quickly a new proposal was made by Bernevig, Hughes and Zhang [11] for the realization of the QSH effect in HgTe-CdTe semiconductor quantum wells. This resulted in the first observation of a material that is insulating in the bulk, is conducting at its edges, and hosts counterpropagating spin currents within it: a topological insulator [12].

The exploration of this field of topological matter started around 1980, drawing upon the concepts of the much older mathematical field of topology. In the last twenty years, the field of topology in condensed matter has become more and more popular. The significance of topological materials was highlighted in 2016, when the Nobel Prize in Physics was awarded to Thouless, Haldane and Kosterlitz "for theoretical discoveries of topological phase transitions and topological phases of matter." Their theoretical work in the 1970's and 1980's has sparked enormous interest in these new types of materials, which

can be used as quantum bits in quantum computers or in new generations of electronics and superconductors.

In this thesis, the electronic properties of graphene and T-graphene are studied. In addition, we determine whether a topological phase exists in different one- and two-dimensional T-graphene lattices. In Chapter 1, the band structures of graphene and graphene nanoribbons are calculated to familiarize ourselves with the tight-binding model. An introduction to topology in condensed matter is given in Chapter 2. In Chapter 3, T-graphene is introduced and the band structure is calculated for different hopping parameters. Additionally, the electronic properties of highly anisotropic T-graphene and several different T-graphene nanoribbons are studied. Finally, the topological properties of a finite-size T-graphene lattice are investigated. Specifically, a magnetic field is introduced to study the topological phases in a two-dimensional T-graphene lattice in Chapter 4 and a one-dimensional T-graphene chain in Chapter 5. The research performed in Chapter 3, 4 and 5 is original, except for a few limiting cases where the results are compared to the literature.

CHAPTER 1

The electronic properties of graphene

1.1 An introduction to graphene

Graphene is a one-dimensional sheet of carbon atoms arranged in a honeycomb lattice. The lattice (see Fig. 1.1a)) contains two equal atoms per unit cell. They belong to two sublattices, A and B, with each atom from sublattice A surrounded by three atoms from sublattice B, and vice versa. The Bravais lattice is a triangular lattice with lattice vectors

$$\boldsymbol{a_1} = \frac{a}{2}\left(\sqrt{3}, 1\right), \qquad \boldsymbol{a_2} = \frac{a}{2}\left(\sqrt{3}, -1\right), \tag{1.1}$$

where a is the C-C bond length (1.42 Å in graphene [13]). The nearest-neighbour vectors are given by

$$\boldsymbol{\delta_1} = \frac{a}{2\sqrt{3}}\left(1, \sqrt{3}\right), \qquad \boldsymbol{\delta_2} = \frac{a}{2\sqrt{3}}\left(1, -\sqrt{3}\right), \qquad \boldsymbol{\delta_3} = \frac{a}{\sqrt{3}}\left(-1, 0\right). \tag{1.2}$$

The first Brillouin zone and lattice vectors $\boldsymbol{b_1}$ and $\boldsymbol{b_2}$ make up the corresponding lattice in reciprocal space (Fig. 1.1b)). The important high-symmetry points in the Brillouin zone are labeled by Γ, K, K$'$ and M.

Graphene has incredible properties, which originate from its sp^2 hybridization and atomic thickness. As we will see in the next section, electrons near the Fermi-level (at the Dirac points) behave as photons because their mass is effectively zero, which results in an extremely high mobility. However, the electrons in graphene move with the Fermi-velocity v_F, which is about 300 times smaller than the speed of light. In addition, each hexagon in graphene has free π-electrons, but due to the zero density of states at the Dirac point, the conductivity is actually quite low at the Fermi-energy. However, the properties of graphene can be changed by doping it, which could make it an excellent conductor or, by opening the band gap, a great transistor [14]. Graphene has incredible strength, stiffness and toughness due to the stable sp^2 carbon bonds [15]. At the same time, it also has elastic properties [16] and is very thin and light. This combination is what makes graphene so special and allows for the use of graphene-based composites in vehicles and optoelectronics [17]. In addition, it absorbs 2.3% of white light [18], which makes it visible but still transparent.

In this chapter, we discuss a tight-binding model for graphene and calculate the band structure. Next, we look at the electronic properties of armchair and zigzag graphene nanoribbons (GNRs).

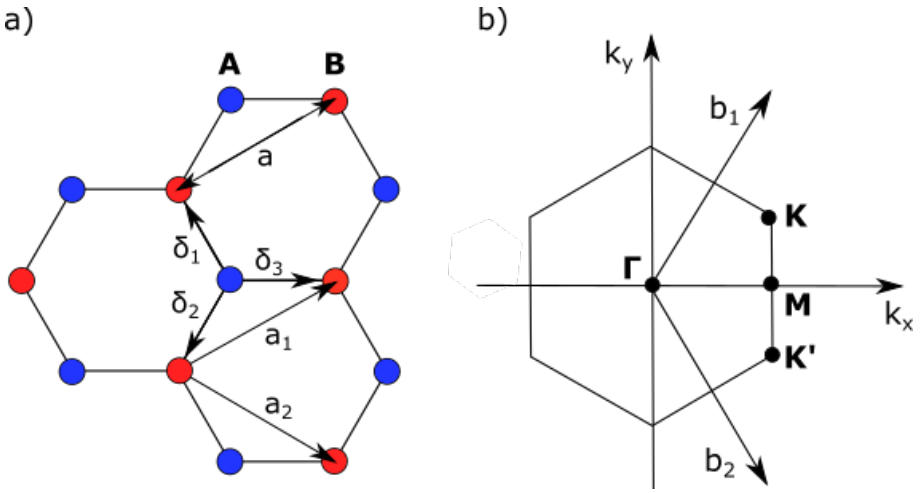

Figure 1.1: a) The geometric structure of a layer of carbon atoms in a honeycomb lattice, with a unit cell consisting of two atoms, A (blue) and B (red), and lattice vectors $\boldsymbol{a_1}$ and $\boldsymbol{a_2}$. b) The corresponding lattice in reciprocal space with the first Brillouin zone and the lattice vectors $\boldsymbol{b_1}$ and $\boldsymbol{b_2}$.

1.2 A tight-binding description of graphene

In the following section, we will use the tight-binding or Hückel model to determine the band structure of graphene. In the Hückel description of conjugated hydrocarbons, molecular orbitals are written as linear combinations of the atomic $2p_z$-orbitals on the C-atoms. The σ-orbitals are not taken into account because they are more strongly bound and simply give rigidity to the material. The electronic properties are determined by the $2p_z$-orbitals.

According to Bloch's theorem, wave functions in crystals can be described as plane waves multiplied by some function that has the same periodicity as the lattice. The Bloch orbitals consisting of A or B atoms are given by

$$\Phi_j(\boldsymbol{k},\boldsymbol{r}) = \frac{1}{\sqrt{N}} \sum_{\boldsymbol{R_j}}^{N} e^{i\boldsymbol{k}\cdot\boldsymbol{R_j}}\, \psi_j(\boldsymbol{r}-\boldsymbol{R_j}), \quad (j=A,B), \tag{1.3}$$

where the summation is taken over the atom site coordinate $\boldsymbol{R_j}$ for the A or B carbon atom, with N the number of unit cells and $\psi_j(\boldsymbol{r}-\boldsymbol{R_j})$ the normalized atomic $2p_z$-state located on atom j at coordinate $\boldsymbol{R_j}$. If we assume that the overall wave function consists of a sum of Bloch waves, we can write the wave function

$$\Psi_i(\boldsymbol{k},\boldsymbol{r}) = \sum_{j=1}^{n} C_{ij}(\boldsymbol{k})\Phi_j(\boldsymbol{k},\boldsymbol{r}). \tag{1.4}$$

Now, we can determine the dispersion relation by evaluating the ith expectation value of the energy using the wave function in Eq. (1.4), such that

$$E_i(\boldsymbol{k}) = \frac{\langle\Psi_i|\hat{H}|\Psi_i\rangle}{\langle\Psi_i|\Psi_i\rangle} = \frac{\sum_{j,j'=1}^{n} H_{jj'}(\boldsymbol{k})C_{ij}^{*}C_{ij'}}{\sum_{j,j'=1}^{n} S_{jj'}(\boldsymbol{k})C_{ij}^{*}C_{ij'}}, \tag{1.5}$$

where $H_{jj'}$ and $S_{jj'}$ are called the transfer and overlap integral matrices respectively, and are defined by

$$H_{jj'}(\boldsymbol{k}) = \left\langle\Phi_j\middle|\hat{H}\middle|\Phi_{j'}\right\rangle \quad \text{and} \quad S_{jj'}(\boldsymbol{k}) = \left\langle\Phi_j\middle|\Phi_{j'}\right\rangle, \qquad (j,j'=A,B). \tag{1.6}$$

Minimizing $E_i(\boldsymbol{k})$ with respect to the coefficients C_{ij}^*, leads to the following matrix equation

$$\begin{pmatrix} H_{AA} - E_i S_{AA} & H_{AB} - E_i S_{AB} \\ H_{BA} - E_i S_{BA} & H_{BB} - E_i S_{BB} \end{pmatrix} \begin{pmatrix} C_{iA} \\ C_{iB} \end{pmatrix} = \begin{pmatrix} 0 \\ 0 \end{pmatrix}. \tag{1.7}$$

In the tight-binding model, the overlap between orbitals on neighbouring atoms is neglected. Therefore, the overlap integral $S_{jj'}$ will be either unity for the same atom or zero for different atoms. Another approximation is made by neglecting the hopping of electrons to non-neighbouring atoms. This is reasonable to first order since the overlap of p_z-orbitals on non-neighbouring atoms is very small. In that case, there is only an integration over a single atom in H_{AA} and H_{BB}, and thus

$$H_{AA} = H_{BB} = \epsilon, \tag{1.8}$$

with ϵ the on-site energy. For the off-diagonal matrix element H_{AB}, we only have to consider the three nearest-neighbour B atoms relative to an A atom, which are denoted by nearest-neighbour vectors δ_n in Eq. (1.2). This yields

$$H_{AB} = -tf(\boldsymbol{k}) \quad \text{and} \quad H_{BA} = H_{AB}^* = -tf^*(\boldsymbol{k}), \qquad \text{where } f(\boldsymbol{k}) = \sum_{n=1}^{3} e^{i\boldsymbol{k}\cdot\boldsymbol{\delta_n}}, \tag{1.9}$$

with t the hopping parameter. The matrix equation then becomes

$$\begin{pmatrix} \epsilon - E_i & -tf(\boldsymbol{k}) \\ -tf^*(\boldsymbol{k}) & \epsilon - E_i \end{pmatrix} \begin{pmatrix} C_{iA} \\ C_{iB} \end{pmatrix} = \begin{pmatrix} 0 \\ 0 \end{pmatrix}. \tag{1.10}$$

This equation can be solved by setting the determinant to zero. Using the definitions of nearest-neighbour vectors $\boldsymbol{\delta_n}$ in Eq. (1.2), we find the final dispersion relation of graphene

$$E(\boldsymbol{k}) = \epsilon \pm t\sqrt{1 + 4\cos^2\left(\frac{ak_y}{2}\right) + 4\cos\left(\frac{ak_y}{2}\right)\cos\left(\frac{\sqrt{3}ak_x}{2}\right)}. \tag{1.11}$$

If we set $\epsilon = 0$, we can calculate and plot the band structure (Fig. 1.2a)). There are two bands and they touch at the K-points. Since every C-atom has one contributing orbital and one electron, the valence band is completely filled and the conduction band is completely empty. The band diagram (Fig. 1.2b)) shows the dispersion relation plotted along the high-symmetry points $\Gamma \to \mathrm{M} \to \mathrm{K} \to \Gamma$. Close to the K-points, where the bands touch, the energy depends linearly on the wave vector. These points are called Dirac points and the density of states in those points is exactly zero. This makes graphene neither a metal nor a semiconductor or insulator, and therefore it is usually referred to as a semimetal or zero-gap semiconductor.

One can show that the energy bands in the region close to the K-points are cones by doing a Taylor expansion around the K-point (or K′-point). First write $\boldsymbol{k} = \boldsymbol{K} + \delta\boldsymbol{k}$ and substitute this into Eq. (1.11). After performing the expansion, only the quadratic terms in δk_x and δk_y are nonzero. We then find

$$\begin{aligned} E(\boldsymbol{k}) &= \pm\, t\sqrt{\frac{3a^2}{4}\left(\delta k_x^2 + \delta k_y^2\right)} \\ &= \pm\, t\,\frac{\sqrt{3}a}{2}\,|\delta\boldsymbol{k}|\,. \end{aligned} \tag{1.12}$$

Using $\boldsymbol{p} = \hbar\boldsymbol{k}$, we rewrite

$$E(\boldsymbol{p}) = \pm v_F\,|\delta\boldsymbol{p}|\,, \qquad \text{with } v_F = \frac{\sqrt{3}at}{2\hbar}. \tag{1.13}$$

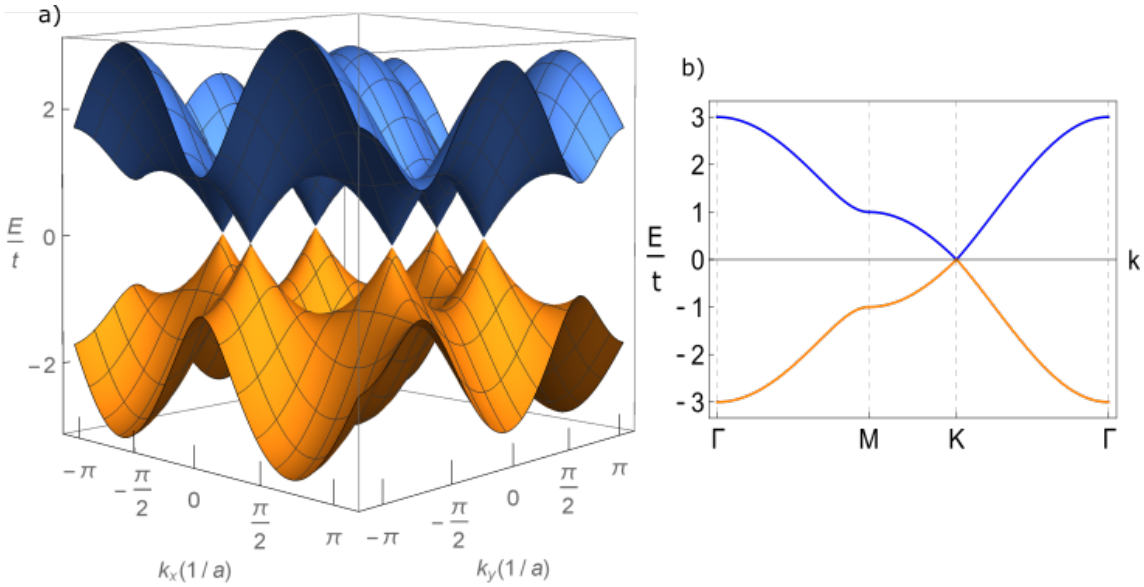

Figure 1.2: a) Electronic dispersion in graphene calculated using the tight-binding model with $\epsilon = 0$. The conduction band (blue) is completely empty and the valence band (orange) is completely filled. b) Band structure of graphene along the high-symmetry points $\Gamma \rightarrow$ M $\rightarrow$ K $\rightarrow \Gamma$ calculated using the tight-binding method. The two bands touch at the Dirac point.

The linear dependence of the energy is strikingly similar to what can be observed in the dispersion relation of photons ($E(\boldsymbol{p}) = c\,|\boldsymbol{p}|$). Electrons in graphene thus behave as if they have no mass and are therefore called massless Dirac fermions. The speed of propagation is nevertheless the Fermi-velocity v_F, which is proportional to the hopping parameter t. Because the mass is effectively zero, the electrons are very mobile, resulting in an extremely low electrical resistivity. This makes graphene particularly suitable for faster electronics and thin, strong, flexible, electrically conducting and transparent films.

1.3 The electronic properties of graphene nanoribbons

The application of graphene in electronic devices calls for successively smaller pieces of graphene. In bulk graphene, the edge effects can be neglected, but when the system size is decreased, the role of the edge states becomes more important. The presence of edges significantly changes the electronic properties of graphene. There are two basic edge shapes: armchair and zigzag (Fig. 1.3). Now, we investigate the band structure of armchair and zigzag ribbons by using the tight-binding approach and discuss the physical consequences of their energy dispersion.

1.3.1 Armchair GNRs

A unit cell of armchair graphene nanoribbons (AGNRs), marked by the dashed rectangle in Fig. 1.3a), spans the entire lattice in the y-direction. The width of the lattice in the x-direction is determined by the number of dimer lines N, such that the unit cell contains $2N$ carbon atoms. After taking into account the tight-binding approximation,

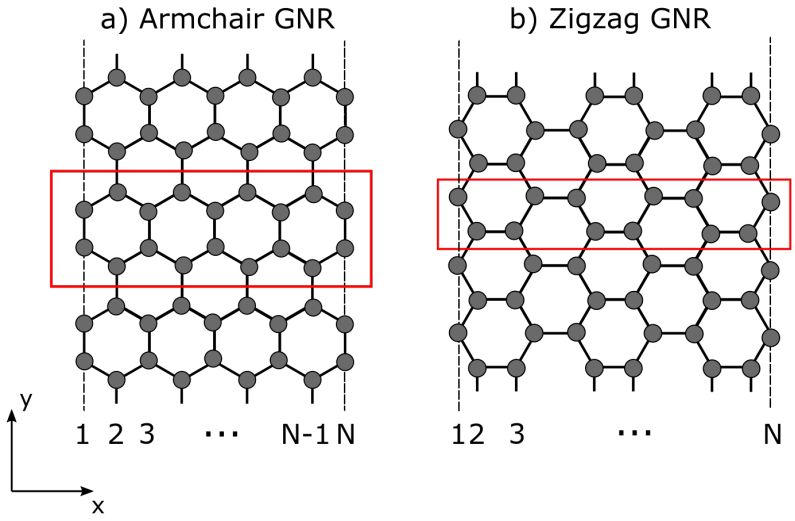

Figure 1.3: Geometric structure of graphene nanoribbons with a) armchair edges and b) zigzag edges. The unit cells are defined by the dashed rectangles.

the corresponding matrix equation is given by

$$E\begin{pmatrix} b_1 \\ b_2 \\ b_3 \\ \vdots \\ b_{2N-1} \\ b_{2N} \end{pmatrix} = \begin{pmatrix} \epsilon & -t & 0 & -t & 0 & \\ -t & \epsilon & -t & 0 & 0 & \\ 0 & -t & \epsilon & -te^{ika} & 0 & \cdots \\ -t & 0 & -te^{-ika} & \epsilon & -t & \\ 0 & 0 & 0 & -t & \epsilon & \\ & & \vdots & & & \ddots \end{pmatrix} \begin{pmatrix} b_1 \\ b_2 \\ b_3 \\ \vdots \\ b_{2N-1} \\ b_{2N} \end{pmatrix}. \tag{1.14}$$

The matrix has a periodicity of 4. One can show (see Ref. [19]) that there exists a diagonal matrix that can transform the tight-binding matrix into another matrix with periodicity 2, which is given by

$$G = \begin{pmatrix} 0 & -te^{-ik/2} & 0 & -t & 0 & \\ -te^{ik/2} & 0 & -t & 0 & 0 & \\ 0 & -t & 0 & -te^{-ik/2} & 0 & \cdots \\ -t & 0 & -te^{ik/2} & 0 & -t & \\ 0 & 0 & 0 & -t & 0 & \\ & & \vdots & & & \ddots \end{pmatrix}, \tag{1.15}$$

where we have set $\epsilon = 0$ and $a = 1$ for convenience. We can now express the eigenvalue problem as a set of two equations

$$\begin{aligned} Ec_m &= -te^{-ik/2}c_{m+1} - tc_{m-1} - tc_{m+3} && \text{for } m \text{ odd}, \\ Ec_m &= -te^{ik/2}c_{m-1} - tc_{m+1} - tc_{m-3} && \text{for } m \text{ even}. \end{aligned} \tag{1.16}$$

If we introduce the notation A_n for odd m and B_n for even m, corresponding to the sublattices A and B, such that $c_1, c_2, c_3, c_4, \ldots \equiv A_1, B_1, A_2, B_2, \ldots$, we can rewrite the equations above as

$$\begin{aligned} EA_n &= -te^{-ik/2}B_n - tB_{n-1} - tB_{n+1}, \\ EB_n &= -te^{ik/2}A_n - tA_{n+1} - tA_{n-1}, \end{aligned} \tag{1.17}$$

with the boundary conditions $A_0 = B_0 = A_{N+1} = B_{N+1} = 0$. Using the ansatz $A_n = Ve^{iqn} + We^{-iqn}$ and $B_n = Xe^{iqn} + Ye^{-iqn}$ and substituting these into the boundary

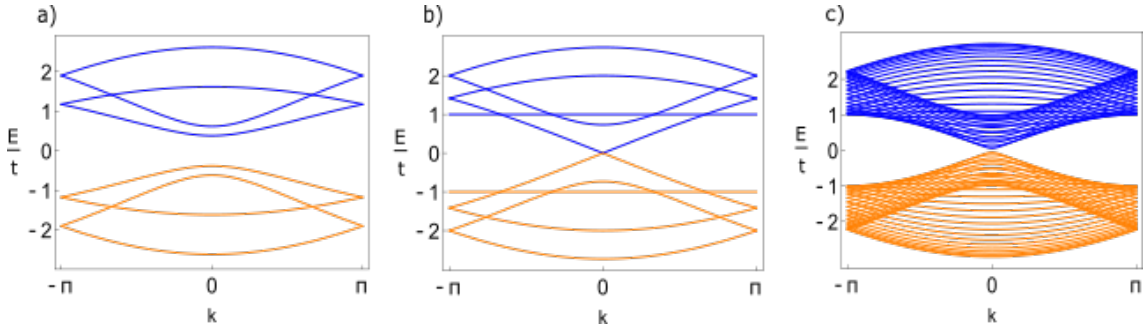

Figure 1.4: a) Band structure of AGNRs with $N = 4$ (semiconducting), b) $N = 5$ (metallic), c) $N = 30$ (semiconducting).

conditions, we find

$$\begin{aligned} &\text{(I)} \quad A_0 = 0 = V + W \implies V = -W, \\ &\text{(II)} \quad B_0 = 0 = X + Y \implies X = -Y. \end{aligned} \tag{1.18}$$

The other boundary conditions then give

$$\begin{aligned} &\text{(III)} \quad V\left(e^{iq(N+1)} - e^{-iq(N+1)}\right) = V2i\sin\left(q(N+1)\right) = 0, \\ &\text{(IV)} \quad X\left(e^{iq(N+1)} - e^{-iq(N+1)}\right) = X2i\sin\left(q(N+1)\right) = 0. \end{aligned} \tag{1.19}$$

We find $\sin\left(q(N+1)\right) = 0$, which yields the trivial solution $q = 0$ and the nontrivial solution $q = r\pi/(N+1)$ with $r = 1, 2, \ldots, N$. Substituting our ansatz into Eq. (1.17) and solving the corresponding 2×2 eigenvalue problem, one obtains for the dispersion relation

$$E(k) = \pm t\sqrt{1 + 4\cos^2\left(\frac{r\pi}{N+1}\right) + 4\cos\left(\frac{r\pi}{N+1}\right)\cos\left(\frac{k}{2}\right)}, \quad \text{with } r \in \mathbb{N}. \tag{1.20}$$

The characteristics of the band structure (Fig. 1.4) depend on the value of N. For $N = 3m - 1$ with $m \in \mathbb{N}$, the conduction and valence band meet at $k = 0$, hence these ribbons have metallic properties. For $N \neq 3m - 1$ there is a band gap, resulting in ribbons with semiconducting properties. The band gap arises from quantum confinement, which can be characterized by $\Delta_{N_a} \sim d_a^{-1}$, where Δ_{N_a} is the band gap belonging to an AGNR with N_a dimer lines [20].

However, first-principle calculations have shown that the size of the band gap is independent of the number of dimer lines N [20], which suggests that AGNRs are always semiconductors. This differs from the tight-binding results because we did not take into account the edge effects, which turn out to play a crucial role. At the edges, the carbon atoms are passivated by hydrogen atoms. Therefore, the σ-bonds between carbon and hydrogen and the on-site energies are different from those in the bulk. In addition, the bond length between carbon atoms at the edge is smaller, which results in an increase of the hopping parameter. This opens up the band gaps of the 3_{m-1}-AGNRs and also changes the band gaps of the 3_m- and 3_{m+1}-AGNRs [20]. If one modifies the matrix equation in Eq. (1.14) to include an extra energy term on the first two and last two entries on the main diagonal, and a different hopping parameter for hopping between carbon atoms at the edge, these additional edge effects can also be described within the tight-binding model.

1.3.2 Zigzag GNRs

The unit cell of zigzag graphene nanoribbons (ZGNRs), marked by the dashed rectangle in Fig. 1.3b), is finite in the x-direction and also contains $2N$ carbon atoms. Constructing and solving the tight-binding eigenvalue equation in a similar way as before gives

$$E(k) = \pm t \sqrt{1 + 4\cos^2\left(\frac{k}{2}\right) + 4\cos\left(\frac{k}{2}\right)\cos(q)}. \tag{1.21}$$

Notice in Eq. (1.21) that q and $k/2$ have switched places compared to Eq. (1.20). This inversion happens because the structure of a ZGNR is essentially the same as the structure of an AGNR rotated over an angle of 90°. Therefore, the k_x- and k_y-directions are also interchanged. The q can then be derived from the relation

$$F(N, q) = 2\cos\left(\frac{k}{2}\right)\sin(q(N+1)) + \sin(Nq) = 0. \tag{1.22}$$

Since q is now a function of both N and k, we cannot solve for q as easily as we did in the case of armchair nanoribbons. However, if we look at Eq. (1.22), we find that it yields N results for $0 \leq |k| \leq k_c$, but only $N-1$ results for $k_c \leq |k| \leq \pi$, where $k_c = 2\arccos\left(\frac{1}{1+1/N}\right)$ [21]. The $N-1$ solutions correspond to the extended states. A good approximation of the $N-1$ solutions to equation (1.22) is given by

$$q = \frac{r\pi}{2N+1}, \qquad \text{with } r = 1, 2, \ldots, N-1. \tag{1.23}$$

The missing solution corresponds to the localized edge state. This edge state distinguishes the zigzag ribbon from the armchair ribbon, which does not have such an edge state. The energy spectrum of the localized edge state can be obtained by analytical continuation (see Ref. [19]) as

$$q \to \begin{cases} \pi + i\eta \equiv q_\pi, & k_c^L \leq |k| \leq \pi, \\ 0 + i\eta \equiv q_0, & \pi \leq |k| \leq k_c^R, \end{cases} \tag{1.24}$$

such that

$$E(k) = \begin{cases} \pm t\sqrt{1 + 4\cos^2\left(\frac{k}{2}\right) - 4\cos\left(\frac{k}{2}\right)\cosh(\eta)}, & \text{for } q_\pi, \\ \pm t\sqrt{1 + 4\cos^2\left(\frac{k}{2}\right) + 4\cos\left(\frac{k}{2}\right)\cosh(\eta)}, & \text{for } q_0, \end{cases} \tag{1.25}$$

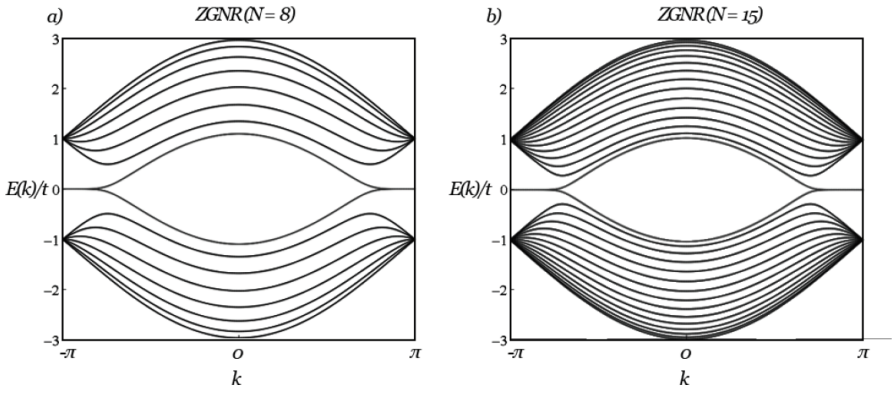

Figure 1.5: a) Band structure of zigzag nanoribbon with $N = 8$ and b) $N = 15$. The band gap is zero for all N, which implies that zigzag nanoribbons are always metallic. Figure from Ref. [22].

where η is the solution to the equation

$$G(N,\eta) = \sinh(N\eta) - 2\left|\cos\left(\frac{k}{2}\right)\right| \sinh(\eta(N+1)) = 0. \tag{1.26}$$

The band gap in the band structure of Z-TGNRs (Fig. 1.5) is zero for all values of N, hence ZGNRs are always metallic. However, in a real nanoribbon, a band gap may arise from a staggered sublattice potential due to spin ordered states at the edges [20]. The spin states on opposite edges have opposite spin and occupy different sublattices. The difference in exchange potential on the two sublattices results in a band gap. Looking at it in another way, we see that the inversion symmetry is broken due to the staggered sublattice, which also results in a band gap [23].

The wave function is completely localized at the edge states for $k = \pi$ and starts to penetrate into the inner sites as k moves away from π, reaching the extended state at $k = 2\pi/3$ in the limit of large N [24]. The (almost) flat bands at the Fermi-level, corresponding to the localized edge states, give rise to a sharp peak in the density of states at the Fermi-level. As a result of the flat band, the kinetic energy term in the Hamiltonian is very small and therefore any potential energy term has a strong effect. This explains why infinitesimally small on-site repulsions could make ZGNRs magnetic at the edges [24]. Note that the armchair ribbon does not exhibit such magnetic behaviour, since the band structure does not contain any flat bands at the Fermi-level.

CHAPTER 2

An introduction to topology in condensed matter

In this chapter, we start with a short introduction to topology and an overview of the relevant symmetries. Next, we study the Su-Schrieffer-Heeger (SSH) model to familiarize ourselves with the concepts and the calculations. Lastly, we discuss the topological importance of introducing a gauge field and introduce Berry phases and Chern numbers.

2.1 Topology and symmetry

This section is broadly based on the chapter *Topology in toy models* from the online course *Topology in Condensed Matter: Tying Quantum Knots* by the TU Delft.

In mathematics, topology is the study of properties that remain intact under continuous deformation of a geometric object. If two objects can be continuously transformed into each other, they are topologically equivalent. A donut and a coffee cup are examples of two topologically equivalent objects, since it is possible to continuously stretch and deform one into the other, because they both have one hole. A property that does not change under continuous transformation is called a topological invariant.

In condensed matter physics, we do not study geometric objects, but physical systems. All the information about interactions in a system is contained in the Hamiltonian. A question we can ask is if two Hamiltonians can be continuously transformed into each other. Without constraints, every Hamiltonian could be continuously transformed into every other Hamiltonian, and all systems would be topologically equivalent. However, when we add constraints, we can divide the Hamiltonians into topological classes, all with a different topological invariant.

If we use the constraint that a system should have an energy gap, we can define the topological invariant as the number of energy levels below zero, or as the number of zero energy crossings. If there is a path that connects two Hamiltonians without closing the gap, they are topologically invariant. However, if the gap must close for the Hamiltonians to continuously transform into each other, the topological invariant changes. This is called a topological phase transition.

We can also restrict ourselves to systems with a certain symmetry. There are several symmetries that can affect the topology of a quantum system. In condensed-matter theory, the three important discrete symmetries are time-reversal symmetry, sublattice or chiral symmetry and particle-hole symmetry.

2.1.1 Time-reversal symmetry

Firstly, we will take a look at time-reversal symmetry. A system is time-reversal symmetric if it can be described by a real Hamiltonian. The Hamiltonian then obeys

$$T^{-1}HT = H, \tag{2.1}$$

with $T = UK$ an anti-unitary matrix, i.e. the product of a unitary matrix U times complex conjugation K. Time-reversal symmetry maps $t \mapsto -t$, which means that $k \mapsto -k$, but $x \mapsto x$.

Time-reversal symmetry makes a real difference in spin-dependent systems, because for systems with spin 1/2, the time reversal operator has the form $T = i\sigma_y K$, such that $T^2 = -1$. A Hamiltonian with this type of time-reversal symmetry obeys the relation $H = \sigma_y H^* \sigma_y$. These Hamiltonians have the property that every eigenvalue is doubly degenerate, which is also known as Kramers' degeneracy. This means that for every zero energy crossing, the topological invariant makes a jump of two and that the topological invariant is constraint to even values.

2.1.2 Sublattice symmetry

Secondly, consider a set of atoms that can be split up into two groups, such that the Hamiltonian only contains nonzero matrix elements between two groups, and not inside each group. In that case, the system has a sublattice symmetry. Sublattice symmetry is also called chiral symmetry, because the chiral operator in the Dirac equation has the same symmetry.

A famous example of a system with sublattice symmetry is graphene, which has two sublattices, A and B. The Hamiltonian of such a system has the form

$$H = \begin{pmatrix} 0 & H_{AB} \\ H_{AB}^\dagger & 0 \end{pmatrix}. \tag{2.2}$$

This matrix obeys the sublattice symmetry relation

$$\sigma_z H \sigma_z = -H, \qquad \text{with } \sigma_z = \begin{pmatrix} 1 & 0 \\ 0 & -1 \end{pmatrix}. \tag{2.3}$$

This means that if $\Psi = (\psi_A, \psi_B)^T$ is an eigenvector with energy E, then $\sigma_z \Psi = (\psi_A, -\psi_B)^T$ is also an eigenvector, but with energy $-E$. In other words, the spectrum is symmetric around zero. The number of positive energy states is equal to the number of negative energy states, and therefore we do not expect a single level to cross zero energy. This means that all Hamiltonians with sublattice symmetry can be continuously deformed into each other.

2.1.3 Particle-hole symmetry

Lastly, let us consider a superconductor with the Hamiltonian

$$H = \sum_{n,m} H_{nm} c_n^\dagger c_m + \frac{1}{2}\left(\Delta_{nm} c_n^\dagger c_m^\dagger + \Delta_{nm}^* c_m c_n\right), \tag{2.4}$$

where the first term describes the dynamics of the electrons and the second term describes the creation and annihilation of Cooper pairs: pairs of electrons bound together due to the electron-phonon interaction in a superconductor. We can rewrite this Hamiltonian

using $C = \left(c_1, \ldots, c_n, c_1^\dagger, \ldots, c_n^\dagger\right)^T$, with c_i the annihilation operators of electrons and $c_i^\dagger$ the creation operators of electrons, such that

$$H = \frac{1}{2} C^\dagger H_{BdG} C, \qquad \text{with } H_{BdG} = \begin{pmatrix} H_0 & \Delta \\ \Delta^* & -H_0^* \end{pmatrix}. \tag{2.5}$$

H_{BdG} is de Bogoliubov-de-Gennes Hamiltonian, with H_0 the single-particle Hamiltonian and Δ the pairing term.

If we think of the creation operators of particles as the annihilation operators of holes, such that there are n annihilation operators of electrons and n annihilation operators of holes, we have doubled the degrees of freedom. Since holes are related to particles, we have an extra symmetry: the particle-hole symmetry. The anti-unitary operator $P = \sigma_x K$ exchanges particles with holes, with the Pauli matrix σ_x acting on the particle and hole blocks. The symmetry relation is

$$P H_{BdG} P^{-1} = -H_{BdG}. \tag{2.6}$$

If $\Psi = (u, v)^T$ is an eigenvector with energy E, then $P\Psi = (v^*, u^*)^T$ is also an eigenvector, but with energy $-E$. Again, the spectrum is symmetric around zero.

2.2 The Su-Schrieffer-Heeger model

We can now apply all these concepts to one of the simplest one-dimensional models: the Su-Schrieffer-Heeger (SSH) model, which is a 1D atom chain with staggered hopping (see Fig. 2.1). The physical structure described by this model is polyacetylene. The staggering occurs naturally in many solids due to Peierls instability [25, 26]. Peierls theorem states that a one-dimensional equally spaced chain with one electron per ion is unstable when it is coupled to phonons. Due to the electron-lattice interaction, the phonons are condensed to form a lattice distortion. At the points in the lattice where the ions form pairs, positive charge accumulates, which attracts the electrons. Because of that, the electrons form a charge density wave, which results in the staggered potential observed in the SSH model. For this section, we will broadly follow Ref. [27].

2.2.1 A tight-binding model of the SSH chain

The Hamiltonian of an SSH chain with N unit cells and two sublattices, A and B, is

$$\hat{H} = -t_w \sum_{m=1}^{N} \left(|m, B\rangle \langle m, A| + h.c. \right) - t_s \sum_{m=1}^{N-1} \left(-t_s |m+1, A\rangle \langle m, B| + h.c. \right) \tag{2.7}$$

The electrons can hop via alternately a weak hopping t_w or a strong hopping t_s. Because of this staggered hopping, the unit cell consists of two atoms, A and B. Since we can split all the degrees of freedom into two groups A and B, such that the Hamiltonian only has

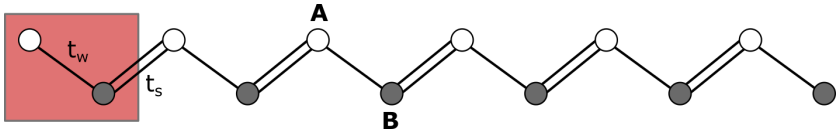

Figure 2.1: Structure of the SSH chain, with two atoms per unit cell (marked by the red rectangle) and staggered hopping. The intracell hopping parameter is t_w and the intercell hopping parameter is t_s.

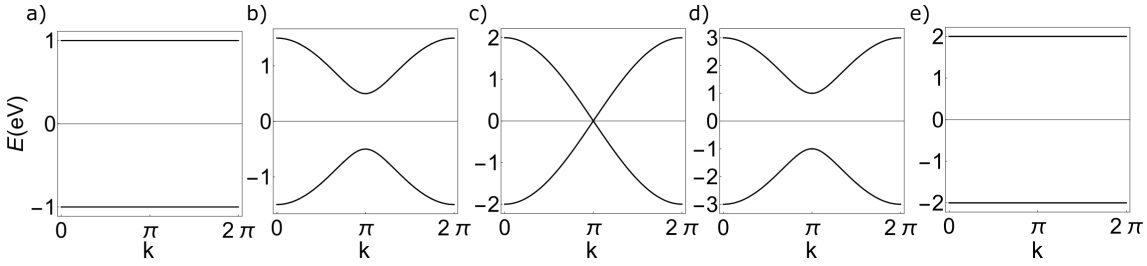

Figure 2.2: The band structure of the SSH chain as a function of k, plotted for a) $t_w = 0$ and $t_s = 1$, b) $t_w = 0.5$ and $t_s = 1$, c) $t_w = 1$ and $t_s = 1$, d) $t_w = 2$ and $t_s = 1$, and e) $t_w = 2$ and $t_s = 0$.

nonzero matrix elements between two groups, and not inside each group, the system is chirally symmetric.

Using Bloch's theorem, we find the bulk Hamiltonian

$$H(k) = \begin{pmatrix} 0 & -t_w - t_s e^{-ik} \\ -t_w - t_s e^{ik} & 0 \end{pmatrix}, \tag{2.8}$$

Solving the eigenvalue problem gives

$$E(k) = \pm\sqrt{t_w^2 + t_s^2 + 2t_w t_s \cos(k)}. \tag{2.9}$$

The band structure is shown in Fig. 2.2 for different values of t_w and t_s. For $t_w < t_s$, there is a band gap, which closes at $t_w = t_s$. The band gap opens up again when $t_w > t_s$. Hence, as long as the hopping amplitudes are staggered, i.e. if $t_w \neq t_s$, there is an energy gap of $2|t_w - t_s|$. If $t_w = t_s$, the SSH chain is conducting.

2.2.2 The fully dimerized SSH chain

We can now look at the two fully dimerized limits. The first case, which we call trivial, is the case where $t_w = 1$ and $t_s = 0$, as in Fig. 2.3a). The energy eigenstates are the even ($E = 1$) and the odd ($E = -1$) superpositions of the two sites from one unit cell that form a dimer. We have

$$\hat{H}\left(|m, A\rangle \pm |m, B\rangle\right) = \pm\left(|m, A\rangle \pm |m, B\rangle\right), \tag{2.10}$$

where the unit cell is labeled by m. We then find $\hat{H}(k) = -\sigma_x$.

In the second case, which is called topological, $t_w = 0$ and $t_s = 1$, as in Fig. 2.3b). Here, the eigenstates are the superpositions of the two sites from neighbouring unit cells that form a dimer. We find

$$\hat{H}\left(|m, B\rangle \pm |m+1, A\rangle\right) = \pm\left(|m, B\rangle \pm |m+1, A\rangle\right). \tag{2.11}$$

The Hamiltonian is now $\hat{H}(k) = -\sigma_x \cos(k) - \sigma_y \sin(k)$. In the trivial case, all energy eigenstates are given by Eq. (2.10). However, a topological, fully dimerized SSH chain has more energy eigenstates than those given in Eq. (2.11). At both ends of the chain there is a single eigenstate at zero energy,

$$\hat{H}\,|1, A\rangle = \hat{H}\,|N, B\rangle = 0. \tag{2.12}$$

These states are called zero-energy edge states. They are at zero energy because the on-site potential is zero and they cannot interact with the neighbouring electron.

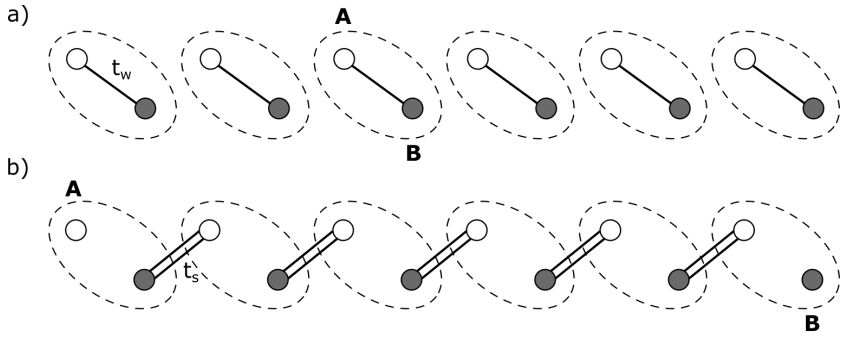

Figure 2.3: The structures of the SSH chain in the fully dimerized limits. a) The trivial case with $t_w = 1$ and $t_s = 0$. b) The topological case with $t_w = 0$ and $t_s = 1$.

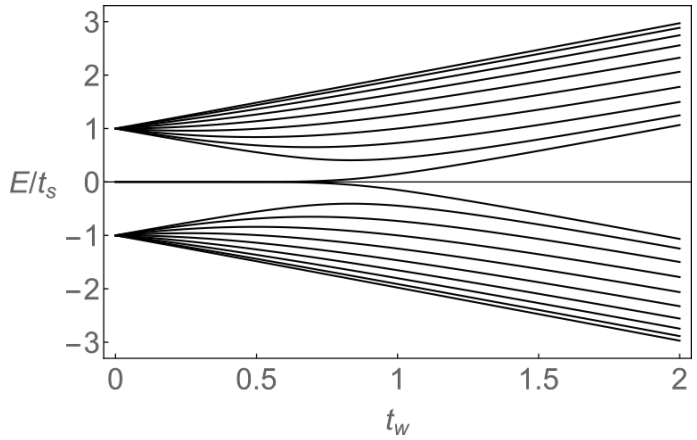

Figure 2.4: The energy eigenvalues of a finite SSH chain with $N = 10$, plotted as a function of t_w with $t_s = 1$. The zero-energy modes stay at zero until $t_w = t_s$ (in the thermodynamic limit).

2.2.3 Moving away from the fully dimerized limit

If we move away from the fully dimerized limit $t_w = 0$ and $t_s = 1$, something interesting happens: the edge states stay at zero until $t_w = t_s$ in the thermodynamic limit. These isolated zero-energy edge modes are protected by the chiral symmetry. This is called the bulk-edge correspondence: the zero-energy edge states can only exist because of a symmetry in the bulk.

In section 2.1.1, we found that the energy spectrum was symmetric because of the sublattice symmetry. This means that the two edge modes must move away from zero simultaneously. Only when the two isolated electrons at the ends of the chain are coupled, i.e. when t_w reaches t_s and the gap closes, the edge modes can move away from zero. In Fig. 2.4, we illustrate this by calculating the energy spectrum of a finite SSH chain as a function of t_w and $t_s = 1$. Here we chose $N = 10$, but for a system with large N, the edge modes only move away from zero at $t_w = 1 = t_s$.

In an SSH system that is not in the fully dimerized limit, the edge state wave functions penetrate exponentially into the bulk. This leads to hybridization of the two edge states, forming a bonding and an anti-bonding state. At half filling, only the bonding eigenstate will be filled. This means that each edge atom carries half an electric charge. In two- or three-dimensional systems, this means that the edges or surfaces are conducting, while the bulk is insulating. The SSH model is therefore the one-dimensional counterpart of a topological insulator.

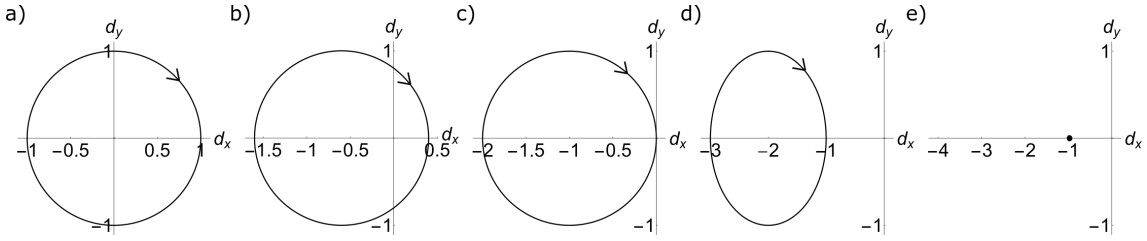

Figure 2.5: The vector $\boldsymbol{d}(k)$ as k goes from 0 to 2π, plotted for a) $t_w = 0$ and $t_s = 1$, with $\nu = 1$, b) $t_w = 0.5$ and $t_s = 1$, with $\nu = 1$, c) $t_w = 1$ and $t_s = 1$, with ν undefined, d) $t_w = 2$ and $t_s = 1$, with $\nu = 0$, and e) $t_w = 2$ and $t_s = 0$, with $\nu = 0$.

2.2.4 The winding number as topological invariant

The dispersion relation gives us a lot of information about the physical properties of the system, but it does not tell us anything about the topology of the system. For that, we need to identify a new quantity: the winding number.

In general, the Hamiltonian $\hat{H}(k)$ for a lattice with two atoms per unit cell without an on-site potential has the form

$$\hat{H}(k) = \begin{pmatrix} 0 & h(k) \\ h^*(k) & 0 \end{pmatrix} = d_x(k)\hat{\boldsymbol{\sigma}}_x + d_y(k)\hat{\boldsymbol{\sigma}}_y + d_z(k)\hat{\boldsymbol{\sigma}}_z. \tag{2.13}$$

For the SSH model, the three components of the vector $\boldsymbol{d}(k)$ are

$$d_x(k) = -t_w - t_s\cos(k); \qquad d_y(k) = -t_s\sin(k); \qquad d_z(k) = 0. \tag{2.14}$$

As the wavenumber runs through the Brillouin zone, the vector $\boldsymbol{d}(k)$ traces out a closed loop, in this case a circle of radius t_s on the d_x, d_y plane, centered at $(-t_w, 0)$.

The topology of this loop can be characterized by a topological invariant, the bulk winding number ν, which counts the number of times the loop winds around the origin. The winding number can be written using the unit vector $\hat{\boldsymbol{d}}(k)$, defined as:

$$\hat{\boldsymbol{d}}(k) = \frac{\boldsymbol{d}(k)}{|\boldsymbol{d}(k)|}. \tag{2.15}$$

The winding number ν is then given by

$$\nu = \frac{1}{2\pi}\int \left(\hat{\boldsymbol{d}}(k) \times \frac{d}{dk}\hat{\boldsymbol{d}}(k)\right)_z dk. \tag{2.16}$$

We can calculate the winding number for different values of t_w and t_s. The closed loop traced by the vector $\boldsymbol{d}(k)$ is shown in Fig. 2.5 for five different values of t_w and t_s. For the topological case $t_w < t_s$, we have $\nu = 1$, for the trivial case $t_w > t_s$, we have $\nu = 0$, and for $t_w = t_s$, ν is undefined, because the vector $\boldsymbol{d}(k)$ moves through the origin. When t_w is increased from 0 to $2t_s$, the system undergoes a topological phase transition at $t_w = t_s$, which is when the winding number changes from $\nu = 0$ to $\nu = 1$.

2.2.5 Exact calculation of the edge states

In order to compute the localization of the edge states in the SSH model, we first need to calculate the zero-energy edge states exactly by solving

$$\hat{H}\sum_{m=1}^{N}\left(a_m\,|m, A\rangle + b_m\,|m, B\rangle\right) = 0, \tag{2.17}$$

using the Hamiltonian given in Eq. (2.7).

Letting the Hamiltonian work on the eigenstate gives $2N$ equations for the amplitudes

$$\begin{cases} -t_w a_m - t_s a_{m+1} = 0; \\ -t_s b_m - t_w b_{m+1} = 0, \end{cases} \qquad \text{for } m = 1, \ldots, N-1, \tag{2.18}$$

with the boundary conditions

$$t_s a_1 = 0; \qquad t_s b_N = 0. \tag{2.19}$$

Solving these equations gives

$$a_m = a_1 \prod_{j=1}^{m-1} \frac{-t_w}{t_s}; \tag{2.20}$$

$$b_m = b_N \prod_{j=m+1}^{N} \frac{-t_w}{t_s}. \tag{2.21}$$

Now, we can write the edge states as

$$|L\rangle = \sum_{m=1}^{N} a_m \, |m, A\rangle \, ; \tag{2.22}$$

$$|R\rangle = \sum_{m=1}^{N} b_m \, |m, B\rangle \, , \tag{2.23}$$

with the coefficients a_m and b_m as in Eq. (2.20) and Eq. (2.21).

To get more insight into the amplitudes of these coefficients, we can calculate the amplitude of a_N and b_1, which are given by

$$a_N = a_1 \prod_{j=1}^{N-1} \frac{-t_w}{t_s} = a_1 \left(\frac{-t_w}{t_s} \right)^{N-1}; \tag{2.24}$$

$$b_1 = b_N \prod_{j=2}^{N} \frac{-t_w}{t_s} = b_N \left(\frac{-t_w}{t_s} \right)^{N-1}. \tag{2.25}$$

Taking the absolute value and rewriting gives

$$|a_N| = |a_1| \left(e^{(\log|t_w| - \log|t_s|)} \right)^{N-1} = |a_1| \, e^{-(N-1)/\xi}; \tag{2.26}$$

$$|b_1| = |b_N| \, e^{-(N-1)/\xi}, \tag{2.27}$$

with $\xi = 1/\left(\log|t_s| - \log|t_w|\right)$. We observe that the amplitudes of the coefficients a_m (b_m) decay exponentially from the left (right) of the chain.

2.3 Gauge fields, Berry phases and Chern numbers

The start of a new era of topological materials was marked by the experimental observation of the quantum Hall effect (QHE) by von Klitzing *et al.* [28]. The QHE is the quantum-mechanical version of the classical Hall effect that was discovered by Edwin Hall

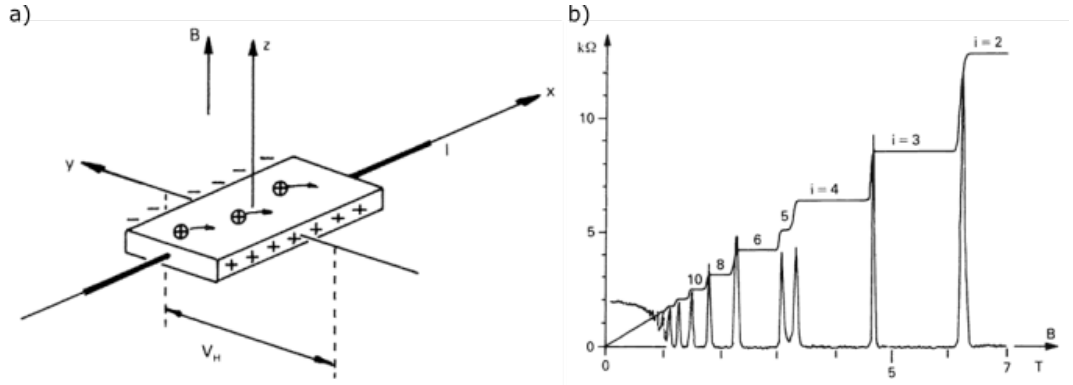

Figure 2.6: a) The setup used by von Klitzing to measure the Hall effect. A perpendicular magnetic field B is applied to a 2DES with a current I running through it, resulting in a net Hall voltage V_H. b) The quantum Hall resistivity plotted as a function of the magnetic field B, showing plateaus at certain ranges of the magnetic field (Kosmos, 1986).

in 1879 [29]. Hall used the setup in Fig. 2.6a), with a current running through a two-dimensional electron system (2DES). When a perpendicular magnetic field is applied, the electrons experience a Lorentz force, which moves them to one side of the material where negative charge accumulates. This leaves equal and opposite charge on the other side, resulting in a transverse electric potential V_H. In the classical picture, the transverse or Hall resistivity depends linearly on the magnetic field.

When a strong magnetic field is applied, the electrons start following circular orbits with the cyclotron frequency $\omega_c = \hbar eB/m$. Due to their quantum-mechanical nature, the energy levels of the electrons are quantized. These so-called Landau levels are separated by an energy difference of $\Delta E = \hbar\omega_c$. This causes the Hall resistivity to exhibit interesting behaviour, as shown in Fig. 2.6b). The Hall resistivity sits on plateaus for certain ranges of the magnetic field. On these plateaus, the resistivity is

$$\rho_{xy} = \frac{h}{\nu e^2}, \qquad \text{with } \nu \in \mathbb{Z}. \tag{2.28}$$

In 1988, Haldane showed with his Haldane model that a net magnetic flux was not a necessary condition for the observation of the QHE [8]. Haldane introduced a magnetic flux in such a way that the net magnetic flux vanished, thereby breaking time-reversal symmetry. This was sufficient to quantize the resistivity as in Eq. (2.28). It turned out that the breaking of time-reversal symmetry was the determining factor in observing the QHE, and not the presence of a net magnetic field.

In the remaining of this section, we will look at the consequences of adding a gauge field and how a two-dimensional quantum system can be characterized topologically, by broadly following Ref. [27].

In momentum space, the eigenfunctions are defined by

$$H(\boldsymbol{k})\,|\psi(\boldsymbol{k})\rangle = E(\boldsymbol{k})\,|\psi(\boldsymbol{k})\rangle\,. \tag{2.29}$$

Upon moving an infinitesimal amount through the Brillouin zone, from $\boldsymbol{k}$ to $d\boldsymbol{k}$, the final state and the initial state will differ by a relative phase

$$\nabla\gamma = i\,\langle\psi(\boldsymbol{k})\,|\nabla_{\boldsymbol{k}}|\,\psi(\boldsymbol{k})\rangle\cdot d\boldsymbol{k} = \boldsymbol{\mathcal{A}}(\boldsymbol{k})\cdot d\boldsymbol{k}, \tag{2.30}$$

where $\boldsymbol{\mathcal{A}}(\boldsymbol{k})$ is the Berry connection. Under a gauge transformation, the relative phase and the Berry connection change as

$$|\psi(\boldsymbol{k})\rangle \to e^{i\phi(\boldsymbol{k})} |\psi(\boldsymbol{k})\rangle ; \qquad \boldsymbol{\mathcal{A}}(\boldsymbol{k}) \to \boldsymbol{\mathcal{A}}(\boldsymbol{k}) + \nabla_{\boldsymbol{k}}\phi(\boldsymbol{k}). \tag{2.31}$$

When moving along a closed curve in momentum space, a Berry phase is picked up, which is given by

$$\gamma = \oint_{\mathcal{C}} \boldsymbol{\mathcal{A}}(\boldsymbol{k}) \cdot d\boldsymbol{k}. \tag{2.32}$$

The Berry phase, unlike the Berry curvature, is gauge invariant, so the pumped charge is invariant as long as the energy gap is preserved.

Now, consider $\mathcal{C}$ to be the boundary of a surface $\mathcal{S}$ within the Brillouin zone. Using Stokes' theorem, we find

$$\gamma = \oint_{\delta\mathcal{S}} \boldsymbol{\mathcal{A}}(\boldsymbol{k}) \cdot d\boldsymbol{k} = \int_{\mathcal{S}} (\nabla \times \boldsymbol{\mathcal{A}}(\boldsymbol{k})) \cdot d\boldsymbol{\mathcal{S}}, \tag{2.33}$$

where $d\boldsymbol{\mathcal{S}}$ is the vector normal to the surface $\boldsymbol{\mathcal{S}}$.

Since these equations are analogous to those for magnetic fields, we can consider the Berry connection as a vector potential, which defines a gauge field in momentum space: the Berry curvature $\boldsymbol{\mathcal{B}}(\boldsymbol{k}) = \nabla \times \boldsymbol{\mathcal{A}}(\boldsymbol{k})$. The Berry phase can then be written as

$$\gamma = \int_{\mathcal{S}} \boldsymbol{\mathcal{B}}(\boldsymbol{k}) \cdot d\boldsymbol{\mathcal{S}}. \tag{2.34}$$

We now know that pumping a magnetic flux through the system, i.e. multiplying the hopping parameters with a phase term, adds a Berry phase to the initial state. When $\mathcal{S} = \mathrm{BZ}$, a closed loop $\delta\mathcal{S}$ corresponds to one cycle around the Brillouin zone which is 2π-periodic. The picked up Berry phase must then be a multiple of 2π, or $\gamma(k_x + 2\pi) = \gamma(k_x) + 2\pi W$. The multiple W defines the Chern number

$$W = \frac{1}{2\pi} \int_{BZ} \boldsymbol{\mathcal{B}}(\boldsymbol{k}) \cdot d\boldsymbol{\mathcal{S}} \tag{2.35}$$

$$= \frac{i}{2\pi} \int_{BZ} (\nabla \times \langle \psi(\boldsymbol{k}) | \nabla_{\boldsymbol{k}} | \psi(\boldsymbol{k}) \rangle) \cdot d\boldsymbol{\mathcal{S}}. \tag{2.36}$$

The analogy with the magnetic field allows us to express the Chern number in terms of the wave function and its derivative. Physically, the Chern number is the same integer as the ν in Eq. (2.28), which is the topological invariant that characterizes the band structure of two-dimensional Quantum Hall systems. When $W = 0$, the system is a topologically trivial insulator, while a nonzero Chern number indicates a topologically nontrivial state. The sources of the Berry flux are the points where the energy bands touch in momentum space. This means that the Berry phase can only be computed if the Hamiltonian has an energy gap.

CHAPTER 3

The electronic and topological properties of T-graphene

3.1 An introduction to T-graphene

In the remaining of this thesis, I will focus on T-graphene (see Fig. 3.1a)). From now on, the research performed in this thesis is original, except for some limiting cases, where the obtained results are compared with the literature.

T-graphene is a one-dimensional sheet of (carbon) atoms arranged in a tetragonal lattice of octagons connected by squares with lattice vectors

$$\boldsymbol{a_1} = a\,(1,0)\,, \qquad \boldsymbol{a_2} = a\,(0,1)\,, \tag{3.1}$$

where a is the lattice constant. A unit cell consists of four atoms, each with three nearest neighbours. In T-graphene, the hopping between atoms within the tetra-ring is characterized by a hopping parameter t_1, and the hopping between nearest-neighbour tetra-rings is described by hopping parameter t_2. In section 3.3 on highly anisotropic T-graphene, we introduce two other hopping parameters, t_1' and t_2', also shown in Fig. 3.1a). The first Brillouin zone and the reciprocal lattice vectors $\boldsymbol{b_1}$ and $\boldsymbol{b_2}$ of T-graphene are shown in Fig. 3.1b). The important high-symmetry points are Γ, X and M.

3.2 A tight-binding description of T-graphene

In this section, we calculate the eigenenergies and show the band structure of T-graphene for different values of t_1 and t_2, with $t_1^{'} = t_1$ and $t_2^{'} = t_2$. Following the tight-binding method described in section 1.2, we write the Hamiltonian for T-graphene

$$H = \begin{pmatrix} 0 & -t_1 & -t_2 e^{-iak_x} & -t_1 \\ -t_1 & 0 & -t_1 & -t_2 e^{iak_y} \\ -t_2 e^{iak_x} & -t_1 & 0 & -t_1 \\ -t_1 & -t_2 e^{-iak_y} & -t_1 & 0 \end{pmatrix}, \tag{3.2}$$

where we have set the on-site energy to zero.

The band structure of T-graphene for five different values of t_1 and t_2 is shown in Fig. 3.2. For $t_2 = 0$, the band structure consists of three flat bands at $E = 0$ and $E = \pm 2t_1$. This is the band structure of isolated tetra-rings. For $0 < t_2 < t_1$, the two bands around the Fermi-energy E_2 and E_3 touch at the M-point and the Γ-point. However, the dispersion is not linear, which means that the density of states is not zero at that point. The other two bands E_1 and E_4 show some dispersion. When $t_2 = t_1$, E_1, E_2 and E_3 cross at the M-point. E_1 and E_3 touch in a Dirac point, while E_2 is flat at the M-point. Similarly, E_2

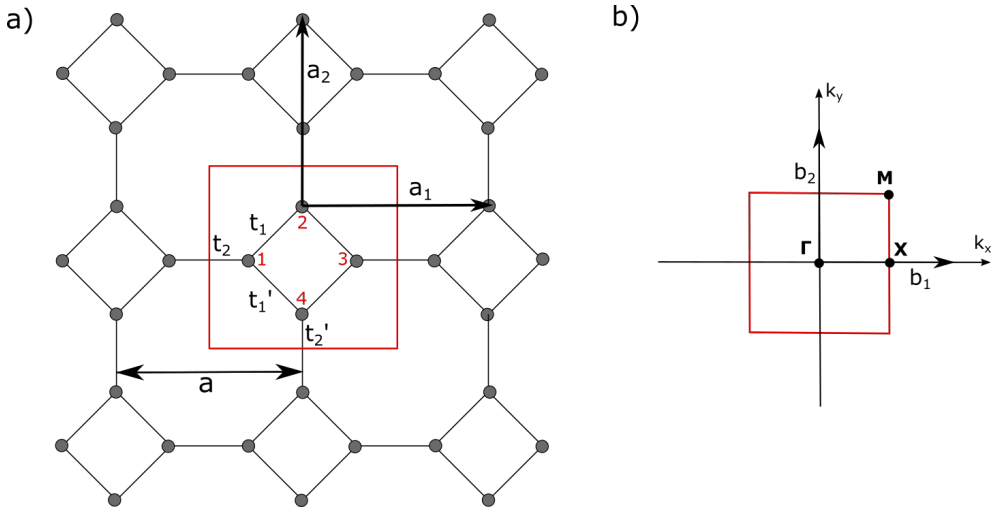

Figure 3.1: a) The geometric structure of T-graphene with four hopping parameters: t_1, t_1', t_2, and t_2', two lattice vectors $\boldsymbol{a_1}$ and $\boldsymbol{a_2}$ and the unit cell marked by the red square. b) The first Brillouin zone (red) and reciprocal lattice vectors $\boldsymbol{b_1}$ and $\boldsymbol{b_2}$ of T-graphene.

and E_4 touch linearly at the Γ-point. The band E_3 crosses this Dirac point without any dispersion. Lastly, for $t_1 < t_2 < 2t_1$, an indirect band gap is opened between E_2 and E_3, which turns into a direct band gap in the limit of $t_2 \to \infty$ (or $t_1 \to 0$). Notice here that E_1 and E_2 form a band structure similar to the structure formed by E_3 and E_4.

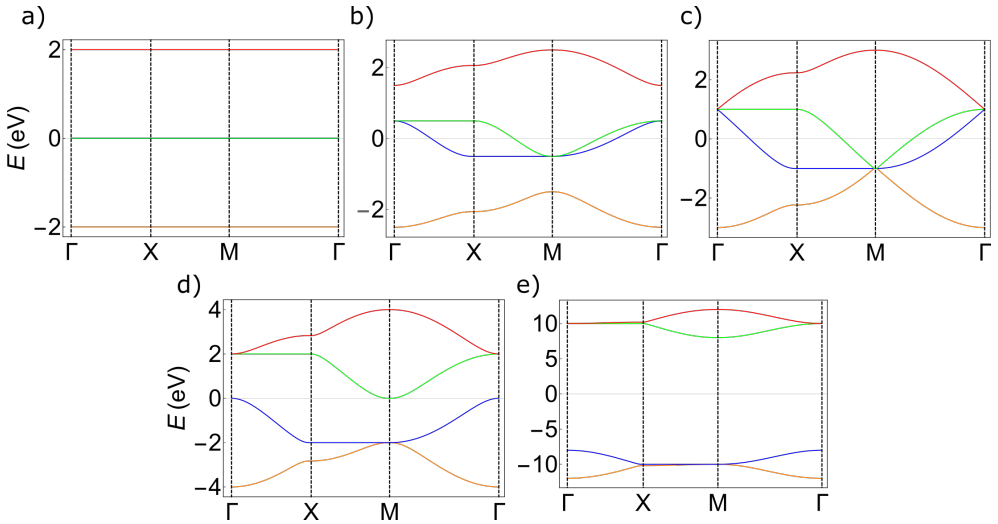

Figure 3.2: The energy eigenvalues of T-graphene (E_1 in orange, E_2 in blue, E_3 in green, and E_4 in red) plotted along the path of high-symmetry points Γ → X → M → Γ, calculated for $t_1 = 1$ and a) $t_2 = 0$, b) $t_2 = 0.5$, c) $t_2 = 1$, d) $t_2 = 2$, and e) $t_2 = 10$.

3.3 Highly anisotropic T-graphene

The energy dispersion of the bands can be modified by introducing uniaxial strain in the lattice. Changing the distance between lattice points is theoretically equivalent to modifying the hopping parameters. In this section, we therefore vary t_1' and t_2' independently of t_1 and t_2, with $t_1 = t_2 = 1$, and study the changes in the band structure. Consider a system where t_1' is varied from 0.5 to 2, while $t_1 = t_2 = t_2' = 1$. In Fig. 3.3a), there are two band crossings between E_3 and E_4 in the y = -x direction and two band crossings between

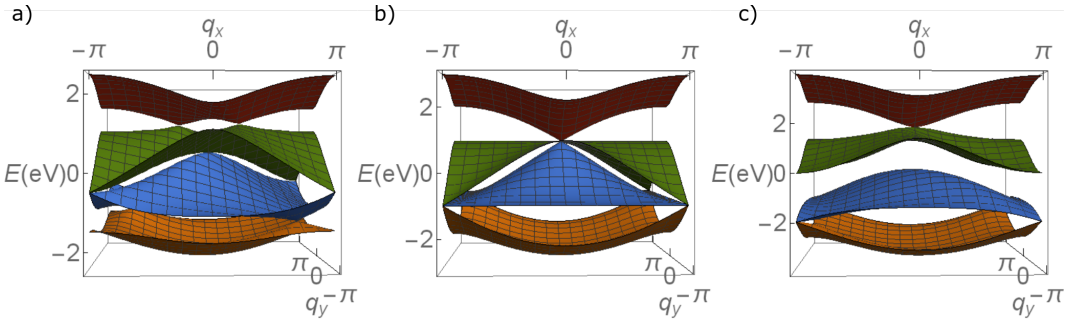

Figure 3.3: The band structures of anisotropic T-graphene (E_1 in orange, E_2 in blue, E_3 in green, and E_4 in red) with $t_1 = t_2 = t_2' = 1$, for a) $t_1' = 0.5$, b) $t_1' = 1.0$, and c) $t_1' = 2.0$.

E_2 and E_3 at the two M-points (-π,π) and (π,-π). At the other two M-points (π,π) and (-π,-π), E_2 and E_3 touch quadratically in one direction and linearly in the other. Another band crossing between these two bands can be found at the Γ-point, where the dispersion relation is parabolic in one direction and linear in the other direction. There are also two band crossings between E_1 and E_2, which have moved away from the high-symmetry points.

Upon increasing t_1' to 1 (see Fig. 3.3b)), we find the same band structure as for normal T-graphene with $t_1 = t_2 = 1$. Note that the two band crossings of E_3 and E_4 have merged into one Dirac cone with E_2. This is similar to what happens when strain is introduced in graphene [30]. The band E_3 crosses at the same point and is now approximately flat around the Γ-point. The two Dirac points between E_1 and E_2 have moved towards the corners of the Brillouin zone and two more Dirac cones have emerged at the two other corners. These Dirac cones have merged with the Dirac cones between E_2 and E_3.

When t_1' is increased even further (see Fig. 3.3c)), we observe that the bands E_2 and E_3 have opened up a gap. The band crossing between E_1 and E_2 has remained and the Dirac cone between E_3 and E_4 has been distorted, such that it is linear in one direction and parabolic in the other.

Now, consider a system where t_2' is varied from 0.5 to 2, while $t_1 = t_1' = t_2 = 1$. For $t_2' = 0.5$ (see Fig. 3.4a)), E_2 and E_3 touch at six different points. The band crossings look similar to the critically tilted Dirac cones that were found in graphene [30], where a flat band crosses a band with dispersion. In this case, there are only critically tilted Dirac points in the direction of q_x and parabolic band crossings in the direction of q_y.

In Fig. 3.4b), t_2' is increased to 1.0, which is the case of normal T-graphene. Upon increasing t_2' even further to 2.0, as shown in Fig. 3.4c), the band crossing between E_3 and E_4 splits and moves to X-points $(\pi, 0)$ and $(-\pi, 0)$. The dispersion is linear in the direction of q_y. In the direction of q_x, E_4 is flat and E_3 is parabolic, which causes an infinite density of states because the upper band is flat. Furthermore, an indirect band gap is opened between E_2 and E_3, which turns into a direct band gap for large t_2'. The band crossings between E_1 and E_2 have merged at the X-points $(0, \pi)$ and $(0, -\pi)$. In this case, the dispersion is linear in the direction of q_y. In the direction of q_x, E_1 is flat and E_2 is parabolic, resulting in a finite density of states.

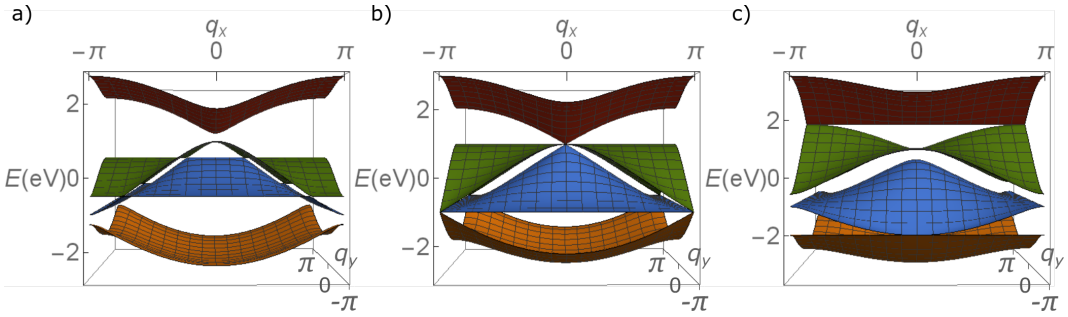

Figure 3.4: The band structures of anisotropic T-graphene (E_1 in orange, E_2 in blue, E_3 in green, and E_4 in red) with $t_1 = t_1' = t_2 = 1$, for a) $t_2' = 0.5$, b) $t_2' = 1.0$, and c) $t_2' = 2.0$.

3.4 Armchair and zigzag T-graphene nanoribbons

It is important to know the structural dependence of the electronic properties of T-graphene for applications in nanotechnology. In this section, we study the different kinds of T-graphene nanoribbons (TGNRs), with $t_1 = t_1'$ and $t_2 = t_2'$. There are two kinds of armchair T-graphene nanoribbons (A-TGNRs), one is symmetric (with even N) and the other one is asymmetric (with odd N). We also study zigzag T-graphene nanoribbons (Z-TGNRs) and bearded T-graphene nanoribbons (B-TGNRs), where we might find protected zero modes.

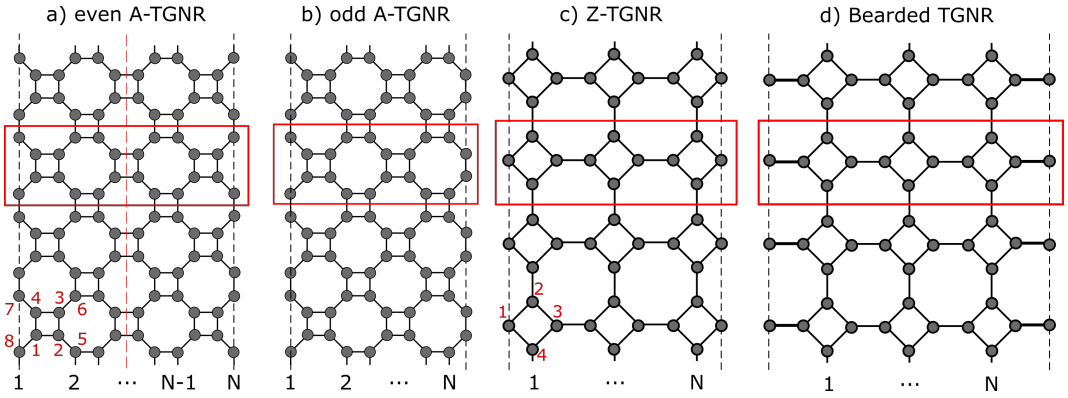

Figure 3.5: The geometric structures of a) even A-TGNRs, b) odd A-TGNRs, c) Z-TGNRs and d) bearded TGNRs. Figure based on Ref. [31].

3.4.1 Even armchair TGNRs

The unit cell of A-TGNRs consists of eight atoms, each with three nearest neighbours. The geometric structures of even and odd A-TGNRs are shown in Fig. 3.5a) and b), respectively. The nearest-neighbour vectors are given by

$$\boldsymbol{\delta_1} = l\,(1,0)\,, \quad \boldsymbol{\delta_2} = l\,(0,1)\,, \quad \boldsymbol{\delta_3} = l\left(-\frac{1}{\sqrt{2}}, -\frac{1}{\sqrt{2}}\right), \quad \boldsymbol{\delta_4} = l\left(-\frac{1}{\sqrt{2}}, \frac{1}{\sqrt{2}}\right), \tag{3.3}$$

with $l = a/(1+\sqrt{2})$. In principle, the distance between atoms within a tetragon can differ from the distance between atoms in neighbouring tetragons. However, this distance would only result in a stretching of the bands, and not in a change of the characteristic electronic properties. We therefore only make use of the freedom in hopping parameters.

The tight-binding Hamiltonian for an A-TGNR with even N is

$$H_{N,EA} = \begin{pmatrix} H_{0,A} & H_{c,A} & 0 & \cdots & 0 \\ H_{c,A}^{\dagger} & H_{0,A} & H_{c,A} & \cdots & 0 \\ 0 & H_{c,A}^{\dagger} & H_{0,A} & \ddots & \vdots \\ \vdots & \vdots & \ddots & \ddots & H_{c,A} \\ 0 & 0 & \cdots & H_{c,A}^{\dagger} & H_{0,A}, \end{pmatrix} \tag{3.4}$$

The matrix $H_{0,A}$ has the form

$$H_{0,A} = \begin{pmatrix} 0 & -t_1\beta_A & 0 & -t_1 & 0 & 0 & 0 & -t_2\alpha_A \\ -t_1\beta_A^* & 0 & -t_1 & 0 & -t_2\alpha_A^* & 0 & 0 & 0 \\ 0 & -t_1 & 0 & -t_1\beta_A^* & 0 & -t_2\alpha_A^* & 0 & 0 \\ -t_1 & 0 & -t_1\beta_A & 0 & 0 & 0 & -t_2\alpha_A & 0 \\ 0 & -t_2\alpha_A & 0 & 0 & 0 & 0 & 0 & -t_1\beta_A \\ 0 & 0 & -t_2\alpha_A & 0 & 0 & 0 & -t_1\beta_A & 0 \\ 0 & 0 & 0 & -t_2\alpha_A^* & 0 & -t_1\beta_A^* & 0 & 0 \\ -t_2\alpha_A^* & 0 & 0 & 0 & -t_1\beta_A^* & 0 & 0 & 0 \end{pmatrix}. \tag{3.5}$$

Here, α_A and β_A are defined by

$$\alpha_A = \exp(i\boldsymbol{k}\cdot\boldsymbol{\delta_3}) = \exp(i\boldsymbol{k}\cdot\boldsymbol{\delta_4}) = \exp\left(\frac{-2\pi ik}{2+\sqrt{2}}\right), \tag{3.6}$$

$$\beta_A = \exp(i\boldsymbol{k}\cdot\boldsymbol{\delta_1}) = \exp\left(\frac{2\pi ik}{1+\sqrt{2}}\right), \tag{3.7}$$

where the momentum vector $\boldsymbol{k} = (2\pi k/a)(1,0)$. This matrix represents the hopping within one unit cell. The matrix $H_{c,A}$ is given by

$$H_{c,A} = \begin{pmatrix} 0 & 0 & 0 & 0 & 0 & 0 & 0 & 0 \\ 0 & 0 & 0 & 0 & 0 & 0 & 0 & 0 \\ 0 & 0 & 0 & 0 & 0 & 0 & 0 & 0 \\ 0 & 0 & 0 & 0 & 0 & 0 & 0 & 0 \\ 0 & 0 & 0 & 0 & 0 & 0 & 0 & 0 \\ 0 & 0 & 0 & 0 & -t_1 & 0 & 0 & 0 \\ 0 & 0 & 0 & 0 & 0 & 0 & 0 & -t_1 \\ 0 & 0 & 0 & 0 & 0 & 0 & 0 & 0 \end{pmatrix}. \tag{3.8}$$

This matrix represents the hopping between different unit cells in the direction with finite length. In the rest of this thesis, we will refer to these types of matrices as sparse matrices with all elements equal to zero, except $H_{c,A}(6,5) = H_{c,A}(7,8) = -t_1$ in this case.

The Hamiltonian for $N = 2$ is given by $H_2 = H_{0,A}$. Solving numerically for the eigenvalues of H_2 yields for the energy bands near the Fermi level

$$\begin{aligned} E_{\pm}(\boldsymbol{k}) &= \mp\frac{1}{2}t_1 \pm \frac{1}{2}\sqrt{5t_1^2 + 4t_2^2 - 4\sqrt{t_1^4 + 2t_1^2t_2^2 + ((\alpha_A^*\beta_A)^2 + (\beta_A^*\alpha_A)^2)t_1^2t_2^2}} \\ &= \mp\frac{1}{2}t_1 \pm \frac{1}{2}\sqrt{5t_1^2 + 4t_2^2 - 4\sqrt{t_1^4 + 2t_1^2t_2^2 + 2\cos(2\pi k)\, t_1^2t_2^2}}. \end{aligned} \tag{3.9}$$

The band structure is shown in Fig. 3.6a) for $t_1 = 2.5$ eV and $t_2 = 3$ eV, and in Fig. 3.6b) for $t_1 = 1$ eV and $t_2 = 2$ eV. We found a critical value for the ratio of hopping parameters $t_c = t_2/t_1$. For $t < t_c$, the two bands around the Fermi-level touch at a point $\boldsymbol{K}$, where

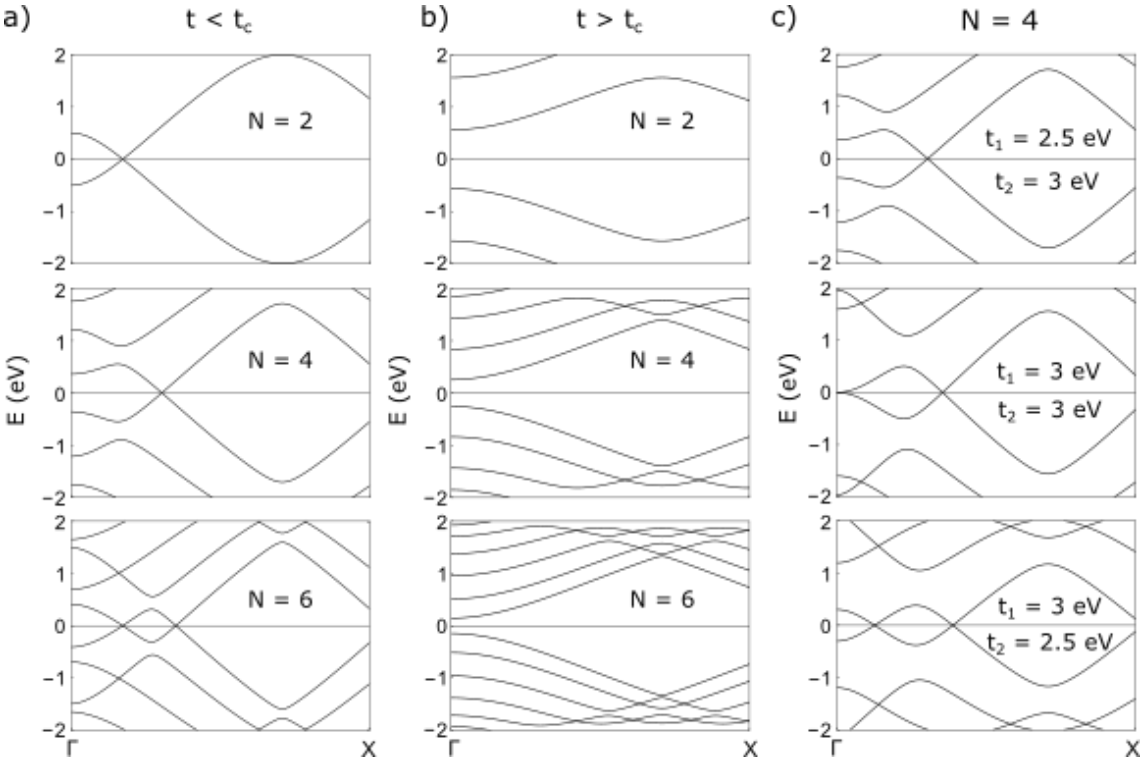

Figure 3.6: The band structure of even A-TGNRs with a) $N = 2, N = 4, N = 6$ for $t_1 = 2.5$ eV and $t_2 = 3$ eV, with b) $N = 2, N = 4, N = 6$ for $t_1 = 1$ eV and $t_2 = 2$ eV, and with c) $N = 4$ for three different combinations of t_1 and t_2.

there is a gap opening for $t > t_c$. This critical value of t depends on N. For $N = 2$, $t_c \approx 1.4$.

By expanding the energy eigenvalues around the Dirac point $\boldsymbol{K}$, i.e. $\boldsymbol{k} = \boldsymbol{K} + \boldsymbol{q}$ with $|\boldsymbol{q}| \ll |\boldsymbol{K}|$, we can obtain the dispersion relation to first order. Solving $E_+(\boldsymbol{K}) = 0$ for $\boldsymbol{K}$ gives

$$|\boldsymbol{K}| = \pm\frac{1}{2\pi}\arccos\left(\frac{t_2^2}{2t_1^2}\right), \tag{3.10}$$

such that we find

$$\boldsymbol{K} = \frac{2\pi K}{a}\begin{pmatrix}1\\0\end{pmatrix} = \frac{1}{a}\cos^{-1}\left(\frac{t_2^2}{2t_1^2}\right)\begin{pmatrix}1\\0\end{pmatrix}, \tag{3.11}$$

$$\boldsymbol{K'} = -\frac{1}{a}\cos^{-1}\left(\frac{t_2^2}{2t_1^2}\right)\begin{pmatrix}1\\0\end{pmatrix}. \tag{3.12}$$

Performing a Taylor expansion around $\boldsymbol{K}$, we find

$$\begin{aligned} E_+(\boldsymbol{k}) &= E_+(\boldsymbol{K}) + \frac{\partial E_+(\boldsymbol{K})}{\partial k}|\boldsymbol{q}| \\ &= 0 + \frac{2\pi t_1^2 t_2^2 \sin(2\pi K)}{\sqrt{5t_1^2 + 4t_2^2 - 4\sqrt{t_1^4 + 2t_1^2t_2^2 + 2\cos(2\pi K)t_1^2t_2^2}}\cdot\sqrt{t_1^4 + 2t_1^2t_2^2 + 2\cos(2\pi K)t_1^2t_2^2}}|\boldsymbol{q}| \end{aligned} \tag{3.13}$$

Calculating $\cos(2\pi K)$ and $\sin(2\pi K)$ separately gives

$$\cos(2\pi K) = \cos\left(2\pi \cdot \frac{1}{2\pi} \arccos\left(\frac{t_2^2}{2t_1^2}\right)\right) = \frac{t_2^2}{2t_1^2} \tag{3.14}$$

$$\sin(2\pi K) = \frac{\sqrt{4t_1^4 - t_2^4}}{2t_1^2} \tag{3.15}$$

Using this, we find

$$\begin{aligned} E_+(\boldsymbol{k}) &= \frac{\pi t_2^2 \sqrt{4t_1^4 - t_2^4}}{\sqrt{5t_1^2 + 4t_2^2 - 4\sqrt{t_1^4 + 2t_1^2t_2^2 + t_2^4}} \cdot \sqrt{t_1^4 + 2t_1^2t_2^2 + t_2^4}} |\boldsymbol{q}| \\ &= \frac{\pi t_2^2 \sqrt{4t_1^4 - t_2^4}}{\sqrt{5t_1^2 + 4t_2^2 - 4(t_1^2 + t_2^2)} \cdot (t_1^2 + t_2^2)} |\boldsymbol{q}| \\ &= \frac{\pi t_2^2 \sqrt{4t_1^4 - t_2^4}}{|t_1|(t_1^2 + t_2^2)} q \\ &= \frac{2\pi t_1^2 t_2^2}{|t_1|(t_1^2 + t_2^2)} \sqrt{1 - \frac{t_2^4}{4t_1^4}} |\boldsymbol{q}| \,. \end{aligned} \tag{3.16}$$

Similarly, we can expand $E_-(\boldsymbol{k})$ around $\boldsymbol{K}$. Summarizing the result for both energy bands, we obtain the linear dispersion relations

$$E_\pm(\boldsymbol{k}) = \pm \frac{2\pi t_1^2 t_2^2}{|t_1|(t_1^2 + t_2^2)} \sqrt{1 - \frac{t_2^4}{4t_1^4}} |\boldsymbol{q}|. \tag{3.17}$$

Upon reintroducing a and $\hbar$ into the dispersion relations, we obtain

$$E_\pm(\boldsymbol{k}) = \pm \frac{2\pi a t_1^2 t_2^2}{\hbar |t_1|(t_1^2 + t_2^2)} \sqrt{1 - \frac{t_2^4}{4t_1^4}} |\boldsymbol{q}| = \pm v_f |\boldsymbol{q}|, \tag{3.18}$$

which is consistent with the result found in Ref. [31].

For $N = 4$ and $N = 6$, the Hamiltonian is given, respectively, by

$$H_4 = \begin{pmatrix} H_{0,A} & H_{c,A} \\ H_{c,A}^\dagger & H_{0,A} \end{pmatrix}; \qquad H_6 = \begin{pmatrix} H_{0,A} & H_{c,A} & 0 \\ H_{c,A}^\dagger & H_{0,A} & H_{c,A} \\ 0 & H_{c,A}^\dagger & H_{0,A} \end{pmatrix}. \tag{3.19}$$

The band structures for $N = 4$ and $N = 6$ are shown in Fig. 3.6a) for $t_1 = 2.5$ eV and $t_2 = 3$ eV, and in Fig. 3.6b) for $t_1 = 1$ eV and $t_2 = 2$ eV. For $N = 4, t_c \approx 1.7$ and for $N = 6, t_c \approx 1.9$. The highest valence band and the lowest conduction band meet at the Fermi level for $t < t_c$. As the width of the nanoribbon increases, the number of Dirac points at the Fermi-level increases as well. For $t > t_c$, there is a band gap. In Fig. 3.6c), the band structures are shown for $N = 4$ for different values of t_1 and t_2.

3.4.2 Odd armchair TGNRs

In the case of odd A-TGNRs, we have to modify the Hamiltonian to

$$H_{N,OA} = \begin{pmatrix} H_{0,A} & H_{c,A} & 0 & \cdots & 0 \\ H_{c,A}^\dagger & H_{0,A} & H_{c,A} & \cdots & 0 \\ 0 & H_{c,A}^\dagger & H_{0,A} & \ddots & \vdots \\ \vdots & \vdots & \ddots & \ddots & H_d \\ 0 & 0 & \cdots & H_d^\dagger & H_1 \end{pmatrix}, \tag{3.20}$$

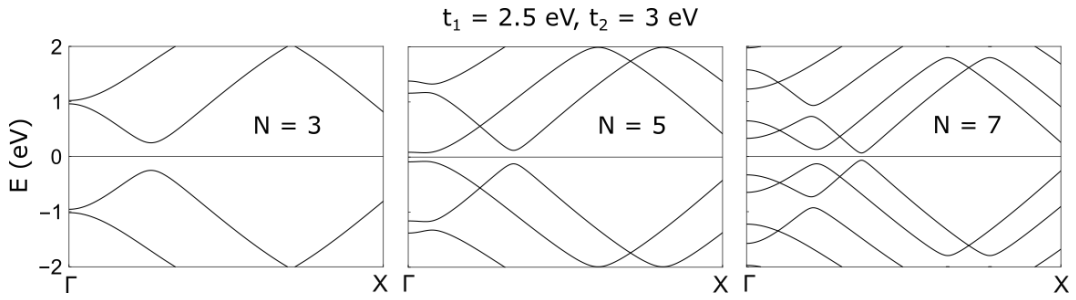

Figure 3.7: The band structures of odd A-TGNRs with a) $N = 3$, b) $N = 5$, c) $N = 7$, for $t_1 = 2.5$ eV and $t_2 = 3$ eV.

where H_1 is a matrix of the form

$$H_1 = \begin{pmatrix} 0 & -t_1\beta_A & 0 & -t_2\alpha_A \\ -t_1\beta_A^* & 0 & -t_2\alpha_A^* & 0 \\ 0 & -t_2\alpha_A & 0 & -t_1\beta_A \\ -t_2\alpha_A^* & 0 & -t_1\beta_A^* & 0 \end{pmatrix}, \tag{3.21}$$

and H_d is a sparse 8×4-matrix, with all elements zero, except $H_d(6,3) = H_d(7,4) = -t_1$.

Fig. 3.7 shows the band structures for $N = 3, N = 5$ and $N = 7$ for $t_1 < t_2$. Compared to symmetric A-TGNRs, the band structure of asymmetric A-TGNRs shows a gap at the Fermi-level for both $t < t_c$ and $t > t_c$. For $t < t_c$, A-TGNRs are therefore found to exhibit oscillating behaviour in their band gap as a function of N. This is probably due to the mirror symmetry in symmetric A-TGNRs, which is broken in asymmetric A-TGNRs [32]. Asymmetric A-TGNRs are therefore always semiconductors, while symmetric A-TGNRs show metallic behaviour for $t < t_c$ and semiconducting behaviour for $t > t_c$. However, this result is based on the tight-binding picture, where we have not taken into account the edge effects. It is therefore possible that first-principles calculations would yield different results, as discussed previously for AGNRs in section 1.3.1.

3.4.3 Zigzag TGNRs

Z-TGNRs (see Fig. 3.5c)) are formed when T-graphene is cleaved at a 45 degree angle. The unit cell consists of four atoms, each with three nearest neighbours. The nearest-neighbour vectors are

$$\boldsymbol{\delta_1} = \frac{1}{\sqrt{2}}(1,1), \qquad \boldsymbol{\delta_2} = \frac{1}{\sqrt{2}}(-1,1), \qquad \boldsymbol{\delta_3} = (0,1), \qquad \boldsymbol{\delta_4} = (1,0). \tag{3.22}$$

The tight-binding Hamiltonian for N unit cells has the form

$$H_{N,Z} = \begin{pmatrix} H_{0,Z} & H_{c,Z} & 0 & \cdots & 0 \\ H_{c,Z}^\dagger & H_{0,Z} & H_{c,Z} & \cdots & 0 \\ 0 & H_{c,Z}^\dagger & H_{0,Z} & \ddots & \vdots \\ \vdots & \vdots & \ddots & \ddots & H_{c,Z} \\ 0 & 0 & \cdots & H_{c,Z}^\dagger & H_{0,Z} \end{pmatrix}, \tag{3.23}$$

where $H_{c,Z}$ is a sparse matrix, with $H_{c,Z}(3,1) = -t_2$, and $H_{0,Z}$ is given by

$$H_{0,Z} = \begin{pmatrix} 0 & -t_1\beta_Z & 0 & -t_1\beta_Z^* \\ -t_1\beta_Z^* & 0 & -t_1\beta_Z^* & -t_2\alpha_Z \\ 0 & -t_1\beta_Z & 0 & -t_1\beta_Z^* \\ -t_1\beta_Z & -t_2\alpha_Z^* & -t_1\beta_Z & 0 \end{pmatrix}. \tag{3.24}$$

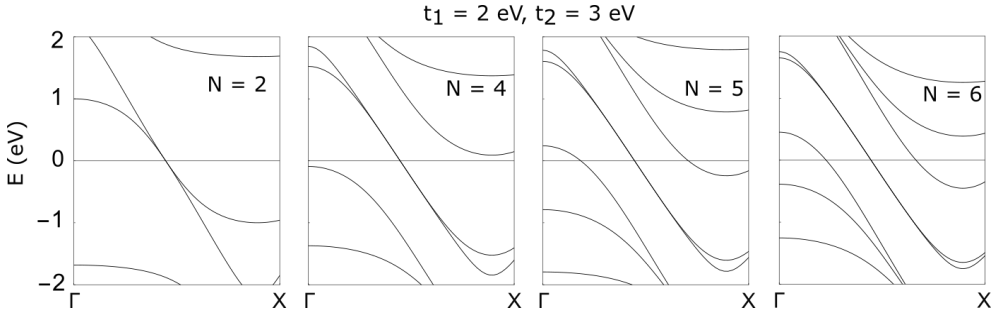

Figure 3.8: The band structure of Z-TGNRs for $t_1 = 2$ eV and $t_2 = 3$ eV, with $N = 2$, 4, 5 and 6.

In the matrix above, α_Z and β_Z are defined by

$$\alpha_Z = \exp(i\boldsymbol{k}\cdot\boldsymbol{\delta_3}) = \exp\left(\frac{2\pi ik}{1+\sqrt{2}}\right), \tag{3.25}$$

$$\beta_Z = \exp(i\boldsymbol{k}\cdot\boldsymbol{\delta_1}) = \exp(i\boldsymbol{k}\cdot\boldsymbol{\delta_2}) = \exp\left(\frac{2\pi ik}{2+\sqrt{2}}\right), \tag{3.26}$$

and the momentum vector $\boldsymbol{k} = (2\pi k/a)(0,1)$.

The band structure of Z-TGNRs is shown in Fig. 3.8. There are electron and hole pockets at the Fermi energy. Our calculations demonstrate that Z-TGNRs have metallic properties, independent of N, due to their zero band gap. This result is consistent with Ref. [31], in which the specific case of T-graphene with $t_1 = 2.525$eV and $t_2 = 2.835$eV was investigated.

3.4.4 Bearded TGNRs

T-graphene nanoribbons can also have a bearded edge (see Fig. 3.5d)). This type of edge is parallel to the zigzag boundary and was first studied by Klein [33]. Bearded edges are unstable in graphene, but they were found to show edge localization in photonic crystals [34, 35]. Partially bearded edges have also been studied in the Kekulé lattice, both theoretically and experimentally [36]. It was shown that the edge mode at the partially bearded edge in a Kekulé lattice is topological when the hopping within the hexagon is stronger than the hopping between hexagons. These findings suggest that introducing bearded edges in T-graphene nanoribbons can lead to topological edge modes.

The Hamiltonian of a B-TGNR is

$$H_{N,B} = \begin{pmatrix} 0 & H_{b1} & 0 & \cdots & & 0 \\ H_{b1}^\dagger & H_{0,Z} & H_{c,Z} & \cdots & & 0 \\ 0 & H_{c,Z}^\dagger & H_{0,Z} & \cdots & & 0 \\ \vdots & \vdots & \vdots & \ddots & & \vdots \\ & & & & H_{0,Z} & H_{b2} \\ 0 & 0 & 0 & \cdots & H_{b2}^\dagger & 0 \end{pmatrix}, \tag{3.27}$$

with $H_{c,Z}$ and $H_{0,Z}$ defined as in section 3.4.3 on Z-TGNRs. H_{b1} and H_{b2} are given by

$$H_{b1} = \begin{pmatrix} -t_2 & 0 & 0 & 0 \end{pmatrix}, \qquad H_{b2} = \begin{pmatrix} 0 \\ 0 \\ -t_2 \\ 0 \end{pmatrix}. \tag{3.28}$$

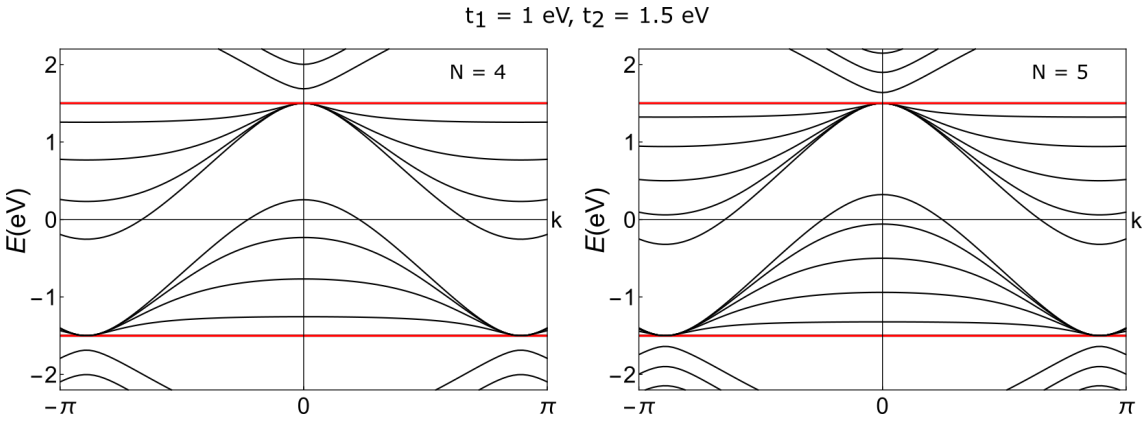

Figure 3.9: Tight-binding band structures of B-TGNRs with $N = 4$ and $N = 5$ for $t_1 = 1$ eV and $t_2 = 1.5$ eV, where the flat bands are marked in red.

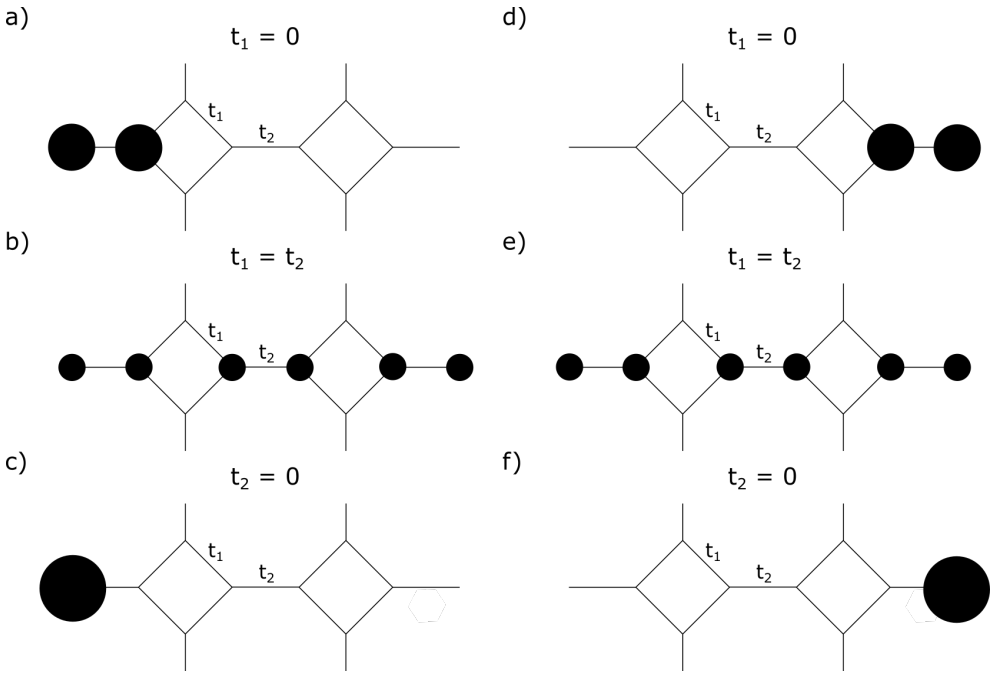

Figure 3.10: The localization of the wave functions ψ corresponding to the flat bands for the left edge atom (a,b,c) and the right edge atom (d,e,f). The area of the disk on site j is proportional to $|\psi_{ij}|^2$, with ψ_{ij} the component of the wave function belonging to energy eigenvalue E_i on that particular site j.

The band structure for B-TGNRs is shown in Fig. 3.9. We find two symmetric flat bands, but no zero modes (except for $t_2 = 0$), which suggests that the wave functions are not localized at the edges for $t_2 \neq 0$. The localization of the two wave functions belonging to the flat bands is shown in Fig. 3.10 for different values of t_1 and t_2. The wave functions are not localized at the edges when t_2 is not exactly zero, but they delocalize immediately upon increasing t_2 from zero to $t_2 = 0.01$. For $t_1 = 0$, we find something that can be described as a dimer localized mode. However, also in this case the wave functions become immediately delocalized when t_1 is increased.

3.5 A finite system of T-graphene with bearded edges

In this last section, we will consider a finite system of T-graphene with bearded edges (see Fig. 3.11a)). The system contains 48 atoms, which are connected by two hopping parameters, t_1 and t_2 as before. We have calculated the energy eigenvalues and plotted them against $t = t_2/t_1$, with t from 0 to 2 (see Fig. 3.11b)). For $t = 0$ (or $t_2 = 0$), there are zero-energy modes. However, when we increase t slightly above zero (as in Fig. 3.11c)), the energy modes move away from zero immediately. In addition, the wave functions corresponding to these zero-energy modes are not localized at the edges for t slightly above zero. This suggests that the edge states are not protected by a chiral symmetry, and hence the system is not topological. A finite-size effect could be that the system is too small, such that the edge atoms hybridize already at a very small value of t. However, upon decreasing t to slightly above zero, the energy modes are still not exactly at zero. Another explanation, which is more likely, is that the edge modes hybridize with the zero-energy modes from the isolated squares and consequently move away from zero directly upon increasing t from zero.

A way to open the gap in the bulk is introducing spin-orbit coupling [37], of which there are two types. The first is intrinsic spin-orbit coupling: a relativistic interaction between the spin and the angular momentum of a particle. In this case, complex next-nearest-neighbour (NNN) hopping leads to the opening of a gap at zero energy. The second type is Rashba spin-orbit coupling [38], which is a combination of intrinsic spin-orbit coupling and an asymmetry in the potential of a crystal. Rashba spin-orbit coupling results in complex nearest-neighbour (NN) hopping and a spin flip, which lifts the spin degeneracy.

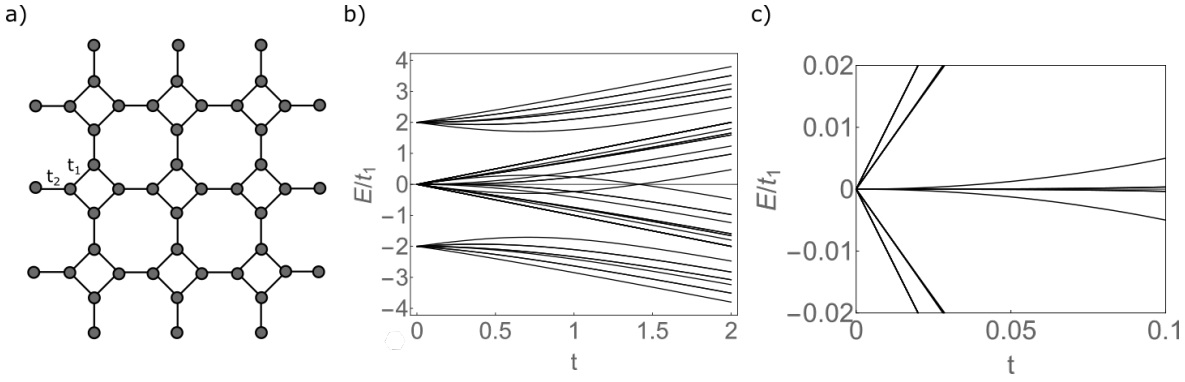

Figure 3.11: a) A finite T-graphene lattice with bearded edges, consisting of 48 atoms and with hopping parameters t_1 and t_2. b) The energy eigenvalues as a function of $t = t_2/t_1$. c) Zoom-in on the zero-energy modes at small t.

Essentially, one can open the band gap in the presence of a strong intrinsic spin-orbit coupling or by applying a perpendicular magnetic field to the system. Both give rise to complex hopping parameters. In the next chapter, we will investigate if any topological properties arise upon including a magnetic flux, i.e. adding a phase to the hopping parameters.

CHAPTER 4

T-graphene in a magnetic field

In this chapter, we study different structures of T-graphene within a magnetic field. We are interested in whether a flux can stabilize a topological phase in T-graphene by preventing the hybridization of the zero-energy edge modes with the zero-energy excitations in the bulk. We first introduce the concept of a magnetic field in a tight-binding model. Next, two different gauge fields are applied to a periodic lattice of T-graphene. The resulting band structures are compared to those of normal T-graphene. Furthermore, we calculate for which flux the zero modes of the isolated squares in a finite system move away from zero. This magnetic field is then applied to bearded T-GNRs. The results are compared with those obtained for bearded T-GNRs without a flux. Lastly, a finite system with bearded edges and a π-flux is studied to comment on the topology of T-graphene.

4.1 The tight-binding model in a magnetic field

In general, the Hamiltonian is given by

$$H(t) = \frac{\boldsymbol{p}^2}{2m} + U(\boldsymbol{r}). \tag{4.1}$$

In the presence of a magnetic field, this changes to

$$\tilde{H}(t) = \frac{(\boldsymbol{p} - q\boldsymbol{A}(t))^2}{2m} + U(\boldsymbol{r}), \tag{4.2}$$

where q is the charge of the particle. The wave function in Eq. (1.3) then changes as

$$\tilde{\psi}_j(\boldsymbol{r} - \boldsymbol{R_j}) = e^{i\frac{q}{\hbar}\int_{R_j}^{r} \boldsymbol{A}(\boldsymbol{r'},t)\cdot d\boldsymbol{r'}} \psi_j(\boldsymbol{r} - \boldsymbol{R_j}), \tag{4.3}$$

which results in new Bloch wave functions

$$\tilde{\Phi}_j(\boldsymbol{k}, \boldsymbol{r}) = \frac{1}{\sqrt{N}} \sum_{\boldsymbol{R_j}}^{N} e^{i\boldsymbol{k}\cdot\boldsymbol{R_j}}\, \tilde{\psi}_j(\boldsymbol{r} - \boldsymbol{R_j}). \tag{4.4}$$

These are now the eigenstates of the full Hamiltonian $\tilde{H}$ with the same energy as before, such that $\tilde{H}(t)\tilde{\psi}_j(\boldsymbol{r} - \boldsymbol{R_j}) = H(t)\psi_j(\boldsymbol{r} - \boldsymbol{R_j})$. When calculating the new hopping parameters, we find

$$\tilde{t}_{R_j R_{j'}} = t_{R_j R_{j'}} e^{i\frac{q}{\hbar}\int_{R_{j'}}^{R_j} \boldsymbol{A}(\boldsymbol{r'},t)\cdot d\boldsymbol{r'}}. \tag{4.5}$$

Therefore, the matrix elements in the Hamiltonian are the same as in the case without a magnetic field, except for the phase factor. It turns out that for electrons, the hopping term t_{ij} can be replaced with $t_{ij}e^{-i\frac{e}{\hbar}\int_i^j \boldsymbol{A}\cdot d\boldsymbol{l}} = t_{ij}e^{-i\Phi/\Phi_0}$, which is called Peierls substitution [39, 40].

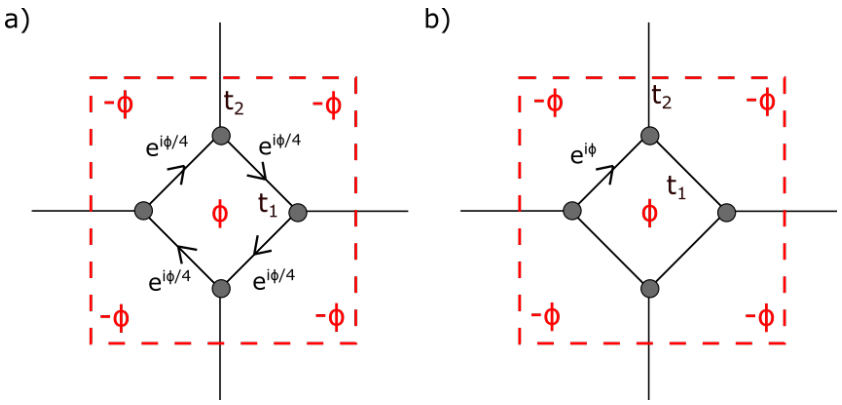

Figure 4.1: The structures of periodic T-graphene with two different fluxes. a) Every intracell hopping adds the same phase $\Phi/4$. b) Only one intracell hopping adds a phase of Φ.

4.2 A T-graphene lattice in different magnetic fields

We consider a periodic T-graphene lattice and apply two different magnetic fields, i.e. multiply the hopping parameter t_1 with two different phase factors. The structures of the lattice with two different fluxes are shown in Fig. 4.1. The unit cells are marked by red squares. We will discuss the two cases individually.

4.2.1 Case 1: Homogeneous flux

In the case of a homogeneous flux, shown in Fig. 4.1a), the flux is chosen in such a way that every intracell hopping has the same phase $\Phi/4$ and the unit cell consists of four atoms. The flux running through the squares is Φ, while the flux through the octagons is $-\Phi$. The Hamiltonian is given by

$$H_{hom} = -\begin{pmatrix} 0 & t_1 e^{i\Phi/4} & t_2 e^{iq_y} & t_1 e^{-i\Phi/4} \\ t_1 e^{-i\Phi/4} & 0 & t_1 e^{i\Phi/4} & t_2 e^{-iq_x} \\ t_2 e^{-iq_y} & t_1 e^{-i\Phi/4} & 0 & t_1 e^{i\Phi/4} \\ t_1 e^{i\Phi/4} & t_2 e^{iq_x} & t_1 e^{-i\Phi/4} & 0 \end{pmatrix}. \tag{4.6}$$

For this system, the band structure was calculated for different values of Φ, t_1, and t_2. The results are shown in Fig. 4.2. The band structures for $\Phi = 0$ were already discussed in Section 3.3. Note that a direct band gap only opens for $t_2 > 2t_1$. At $\Phi = \pi$, there are eight band crossings present for $t_2 < \sqrt{2}t_1$: four between the upper two bands and four between the lower two bands. The dispersion relation at these points is linear in the x- and y-direction. Only at $t_2 = \sqrt{2}t_1$, the gap closes. This occurs in the middle and at the corners of the Brillouin zone with five extra band crossings between the bands around the Fermi energy. A band-inversion takes place before the gap opens again at $t_2 > \sqrt{2}t_1$.

Interestingly, the band structures for $\Phi = 2\pi$ are similar to the ones for $\Phi = 0$, but then reflected in the k-axis. For $\Phi = 4\pi$, the results are the same as for zero flux. Furthermore, the band structures at $\Phi = 3\pi$ (not shown here) are equal to those at $\Phi = \pi$. We thus find that the band structure is 4π-periodic, which is consistent with the matrix H_{hom} in Eq. (4.6) (which is at the most 8π-periodic).

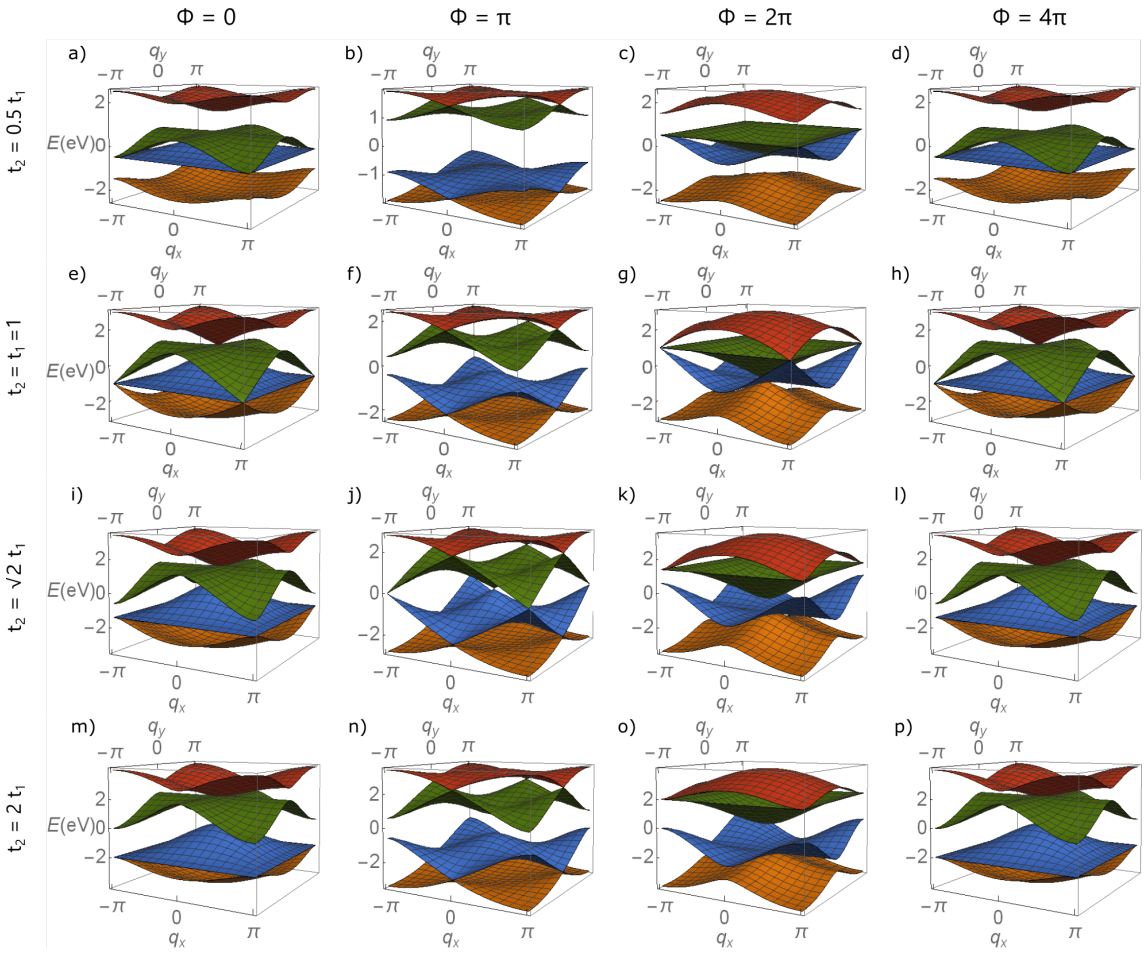

Figure 4.2: The band structure of periodic T-graphene with a homogeneous flux for $t_1 = 1$ and a-d) $t_2 = 0.5t_1$, e-h) $t_2 = t_1 = 1$, i-l) $t_2 = \sqrt{2}t_1$, and m-p) $t_2 = 2t_1$, with a flux of (a,e,i,m) $\Phi = 0$; (b,f,j,n) $\Phi = \pi$; (c,g,k,o) $\Phi = 2\pi$; and (d,h,l,p) $\Phi = 4\pi$.

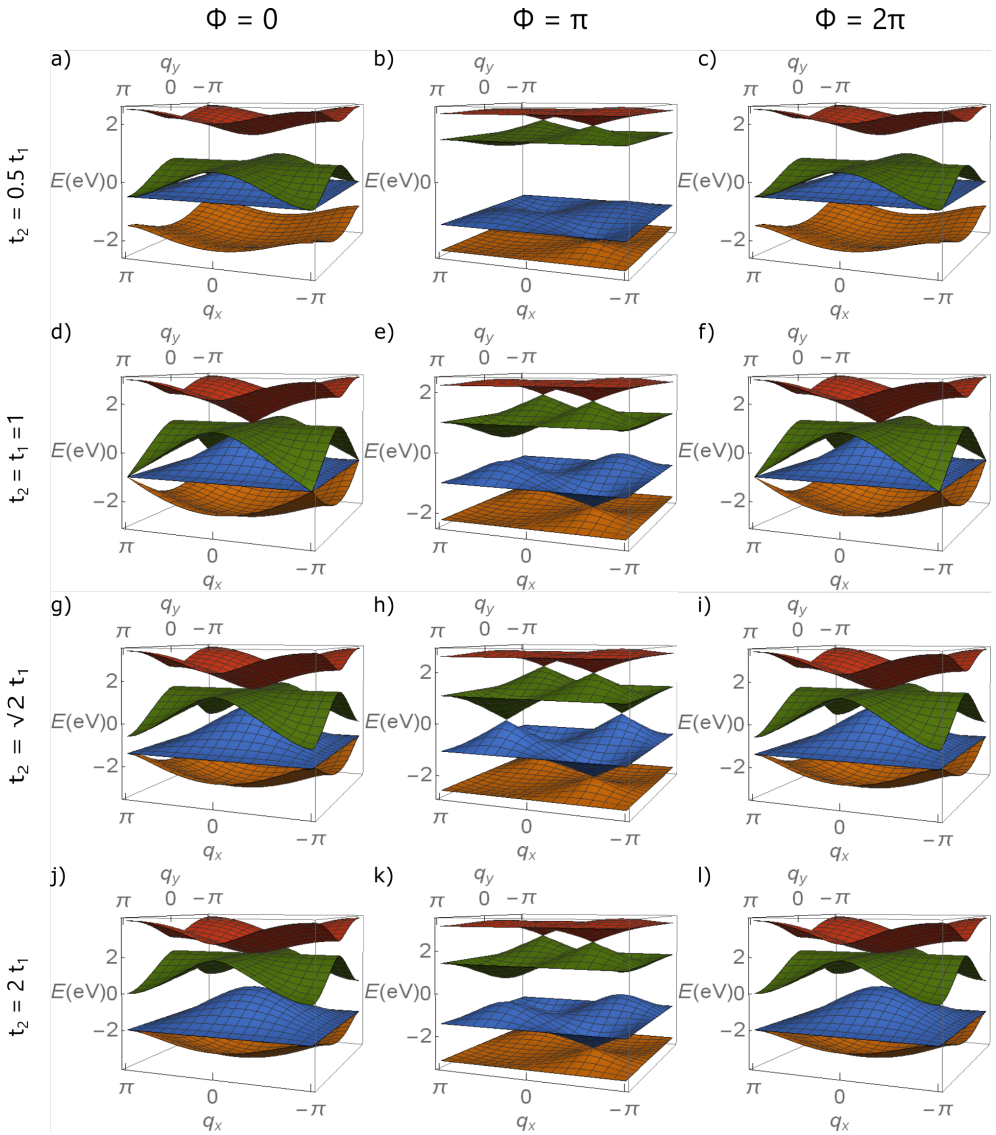

Figure 4.3: The band structure of periodic T-graphene with an inhomogeneous flux, for $t_1 = 1$ and a-c) $t_2 = 0.5t_1$, d-f) $t_2 = t_1 = 1$, g-i) $t_2 = \sqrt{2}t_1$, and j-l) $t_2 = 2t_1$ with a flux of (a,d,g,j) $\Phi = 0$; (b,e,h,k) $\Phi = \pi$; and (c,f,g,l) $\Phi = 2\pi$.

4.2.2 Case 2: Inhomogeneous flux

The same calculations were done for a slightly different system with inhomogeneous flux, where only one intracell hopping is multiplied with the phase factor $e^{i\Phi}$, as is shown in Fig. 4.1b). Note that this results in exactly the same flux Φ running through the squares as in the homogeneous case. The Hamiltonian is

$$H_{inhom} = -\begin{pmatrix} 0 & t_1 e^{i\Phi} & t_2 e^{iq_y} & t1 \\ t_1 e^{-i\Phi} & 0 & t_1 & t_2 e^{-iq_x} \\ t_2 e^{-iq_y} & t_1 & 0 & t_1 \\ t_1 & t_2 e^{iq_x} & t_1 & 0 \end{pmatrix}. \tag{4.7}$$

In Fig. 4.3, the band structures of T-graphene with an inhomogeneous flux are shown for different values of t_1, t_2, and Φ. For $\Phi = 0$, the gap is closed for $t_2 < t_1$. At $t_1 = t_2$, the upper band touches the blue band linearly in at least the x- and y-direction, with the green band approximately flat in between. Upon increasing t_2, a gap is opened. For $\Phi = \pi$, there are four band crossings when $t_2 < \sqrt{2}t_1$. Upon increasing t_2, the bands

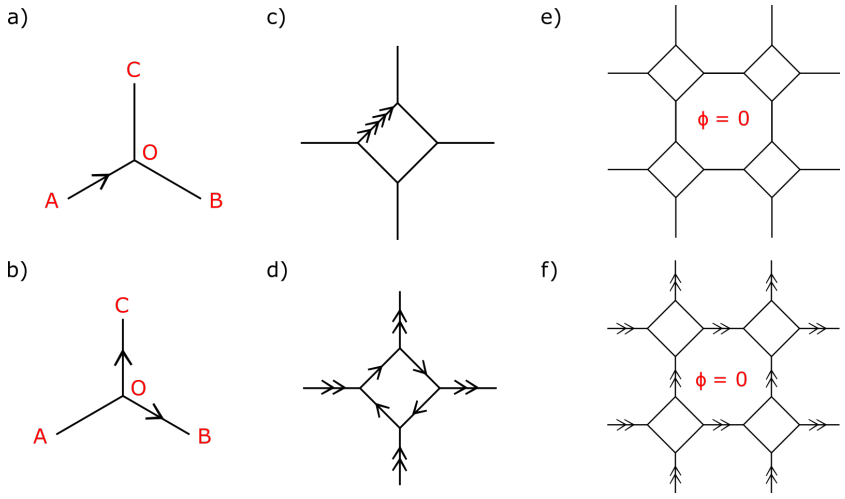

Figure 4.4: The example system a) before the gauge transformation and b) after the gauge transformation. The same technique was applied to the system in c) and yielded d). The difference between c) and d) is the structure in f), which we compare to the structure in e).

around the Fermi energy move closer towards zero and close the gap at $t_2 = \sqrt{2}t_1$ with two extra band crossings. For $t_2 > \sqrt{2}t_1$, a gap is opened again. The band structures for $\Phi = 2\pi$ are equal to those for $\Phi = 0$, so the band structures are 2π-periodic. This result is consistent with the matrix H_{inhom} in Eq. (4.7), which is manifestly 2π-periodic.

For both types of flux, a phase of Φ is picked up when going around the square loop (or a phase of $-\Phi$ when going around the octagonal loop). We would therefore expect to see the same band structures. However, the band structures for T-graphene with an inhomogeneous flux are different. First, notice the difference in periodicity: 2π in the case of inhomogeneous flux and 4π in the case of homogeneous flux. Next, the bands also look different. On the other hand, the differences in the band structure could also be caused by a shift in the Brillouin zone, which may happen when a magnetic field is introduced.

In order to determine whether the two systems are the same, we have to try to transform one into the other. Take the system in Fig. 4.4a) as an example, which has the Hamiltonian

$$H = \left(te^{i\phi}c_A^\dagger c_0 + tc_B^\dagger c_0 + tc_C^\dagger c_0\right) + h.c., \tag{4.8}$$

where t is the hopping parameter and $c^{(\dagger)}$ is the creation (annihilation) operator in second quantization. We can move the phase from the bond between A and 0 by using the gauge transformation $c_0 \to c_0 e^{-i\phi}$. The Hamiltonian then changes to

$$H = \left(tc_A^\dagger c_0 + te^{-i\phi}c_B^\dagger c_0 + te^{-i\phi}c_C^\dagger c_0\right) + h.c., \tag{4.9}$$

which corresponds to the system with the flux drawn as in Fig. 4.4b). Notice that the minus sign in the phase factor determines the direction of the flux arrow. We can apply this technique to T-graphene with inhomogeneous flux, which is drawn in Fig. 4.4c), where we have replaced the phase Φ with four times the phase $\Phi/4$. The result, shown in Fig. 4.4d), differs from T-graphene with homogeneous flux in that the intercell hoppings are now multiplied with a phase factor $e^{i\Phi/2}$. Notice that determining whether T-graphene with homogeneous flux is equal to T-graphene with inhomogeneous flux, effectively is the same as determining whether the two systems in Fig. 4.4e) and f) are equal.

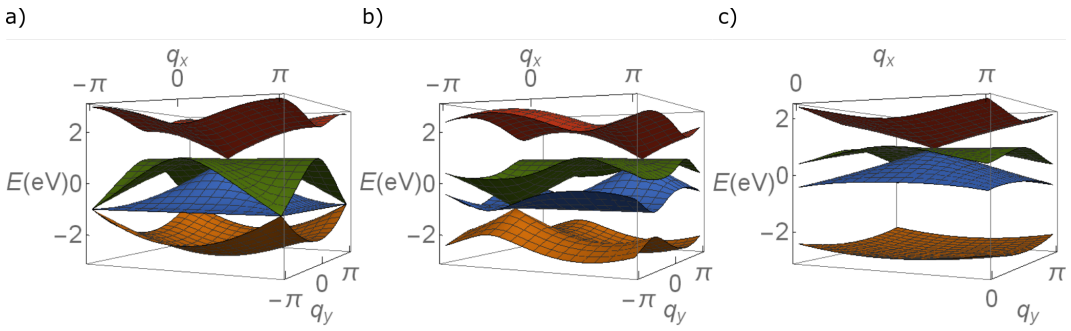

Figure 4.5: The band structure of the systems in a) Fig. 4.4e), and b) Fig. 4.4f). c) is the zoomed-in version of b).

The Hamiltonian

$$H_{dif} = -\begin{pmatrix} 0 & t_1 & t_2 e^{-i\Phi/2} e^{iq_y} & t_1 \\ t_1 & 0 & t_1 & t_2 e^{i\Phi/2} e^{-iq_x} \\ t_2 e^{i\Phi/2} e^{-iq_y} & t_1 & 0 & t_1 \\ t_1 & t_2 e^{-i\Phi/2} e^{iq_x} & t_1 & 0 \end{pmatrix} \tag{4.10}$$

describes the structure in Fig. 4.4e) for a phase $\Phi = 0$ and the structure in Fig. 4.4f) for a phase $\Phi \neq 0$. The band structures for $\Phi = 0$ and $\Phi = \pi$ are shown in Fig. 4.5a) and b) respectively. They are clearly different, but seem to have the same characteristics. However, when zooming in on Fig. 4.5b), such that there is only one band crossing (see Fig. 4.5c)), we can observe that they are different. The counter-intuitive behaviour of the flux means that the choice of flux is important and that the two cases are intrinsically different. The reason for this is that the two cases are not equivalent by a gauge transformation, which means that the two configurations cannot arise from the same magnetic field. Further note that the symmetry of the two configurations is different: four-fold rotation symmetry is preserved in case 1 (even for nonzero values of Φ), while it is broken in case 2.

Also notice that a netto flux accumulates at the boundaries for the structure in Fig. 4.4f). After one unit cell, we obtain a flux $\Phi/2$ at the upper and right boundary. For periodic boundary conditions, a flux of $\Phi = 4\pi$ is necessary, since $e^{i4\pi/2} = e^{i2\pi} = e^{i0\pi}$. This can explain why we find a 4π-periodicity instead of a 2π-periodicity. From here, we only consider T-graphene systems with a homogeneous flux.

4.3 A finite system with flux

Now, consider a finite system of T-graphene with flux (see Fig. 4.6a)). For this, we have adjusted the model discussed in section 3.5, by removing the bearded edges and adding a phase factor $e^{i\Phi/4}$ to the hopping parameters. We do not expect any zero-energy edge modes, since this finite system has no isolated edge atoms. However, when $t_2 = 0$, the isolated squares have two modes at zero, which can hybridize with the zero-energy edges modes in a system with bearded edges. Including a flux would move the bands belonging to the square plaquettes away from zero. In Fig. 4.7, we have plotted the energy spectrum as a function of t_2 for different values of Φ, where t_1 is taken as unity.

We can clearly see that the spectra are 2π-periodic, which is different from the 4π-periodicity we found for a periodic system. However, the spectrum of a finite-size system is symmetric around zero. Therefore, a reflection about $E = 0$ does not result in a different band structure here. At $\Phi = \pi + 2\pi k$, with k an integer, the zero modes emerging from the bulk have moved away from zero. Consequently, upon including a flux of $\Phi = \pi$ in a

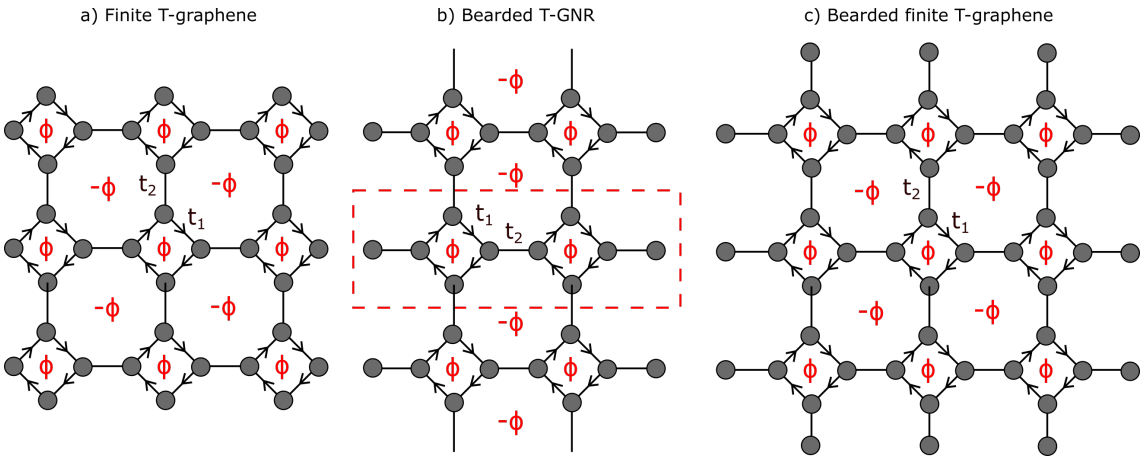

Figure 4.6: T-graphene with a flux in a) a finite system, b) a T-graphene nanoribbon with bearded edges, and c) a finite system with bearded edges. The unit cell in b) is marked by the red dashed rectangle.

T-graphene lattice with bearded edges, we expect that the zero-energy edge modes in a topologically nontrivial phase cannot hybridize with other zero-energy modes and stay at zero, until the coupling is strong enough for them to move away from zero symmetrically.

4.4 Bearded T-GNRs with flux

Now, we consider a B-TGNR under a staggered magnetic flux. The structure is shown in Fig. 4.6b), with the unit cell marked by the red rectangle. To describe this system, we use a tight-binding Hamiltonian similar to the one introduced in section 3.4.4, with the hopping parameters now multiplied by a phase factor $e^{i\Phi/4}$.

In Fig. 4.8, the energy eigenvalues $E(k)$ are plotted as a function of k for different values of t_1 and t_2, with $\Phi = \pi$. At $t_2 = 0$, there are two degenerate nonzero energy bands (because of the isolated square plaquettes) and a zero-energy band which is doubly degenerate (because of the bearded edge atoms). Upon increasing t_2, the bands become dispersive and the two zero-energy bands also move away from zero. For $k \neq 0$ and $k \neq \pi$, the dispersion is nonzero. This means that the zero modes can move along k on the edge and are not localized. The gap is opened at $t_2 = t_1$. As t_2 increases to values much larger than t_1, the energy values form two bands again, one positive and one negative: the zero-energy bands have merged into the bulk bands. The band structure does not show any topological features.

When comparing Fig. 4.8d) with the results for bearded T-GNRs without a magnetic field (see Fig. 4.8), we notice the absence of flat bands in the band structure for $\Phi = \pi$ (except for $t_2 = 0$ or $t_1 = 0$). Furthermore, a direct band gap is present instead of the indirect band gap we found for the case with zero flux. The band structure of the system with flux is also symmetric around zero, while that is not the case when $\Phi = 0$.

4.5 A finite system with bearded edges and flux

To determine whether T-graphene with bearded edges and a π-flux is topological, consider such a finite system of 3×3 unit cells with bearded edges (see Fig. 4.6c)). In this section, we use the model discussed in section 3.5, with the hopping parameters now multiplied by a phase factor $e^{i\Phi/4}$. The energy spectrum as a function of t_2 is shown in Fig. 4.9a), with

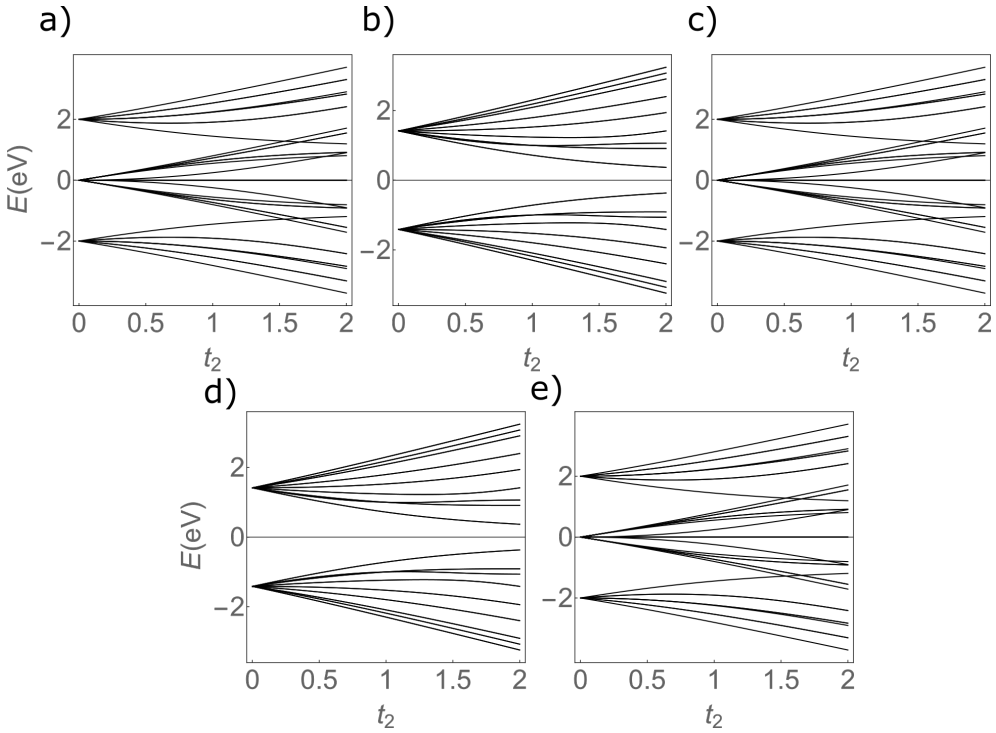

Figure 4.7: The energy spectrum of a finite system of T-graphene plotted as a function of t_2 with $t_1 = 1$ for a) $\Phi = 0$, b) $\Phi = \pi$, c) $\Phi = 2\pi$, d) $\Phi = 3\pi$, and e) $\Phi = 4\pi$. Figures a), c) and e) are equal, and so are b) and d).

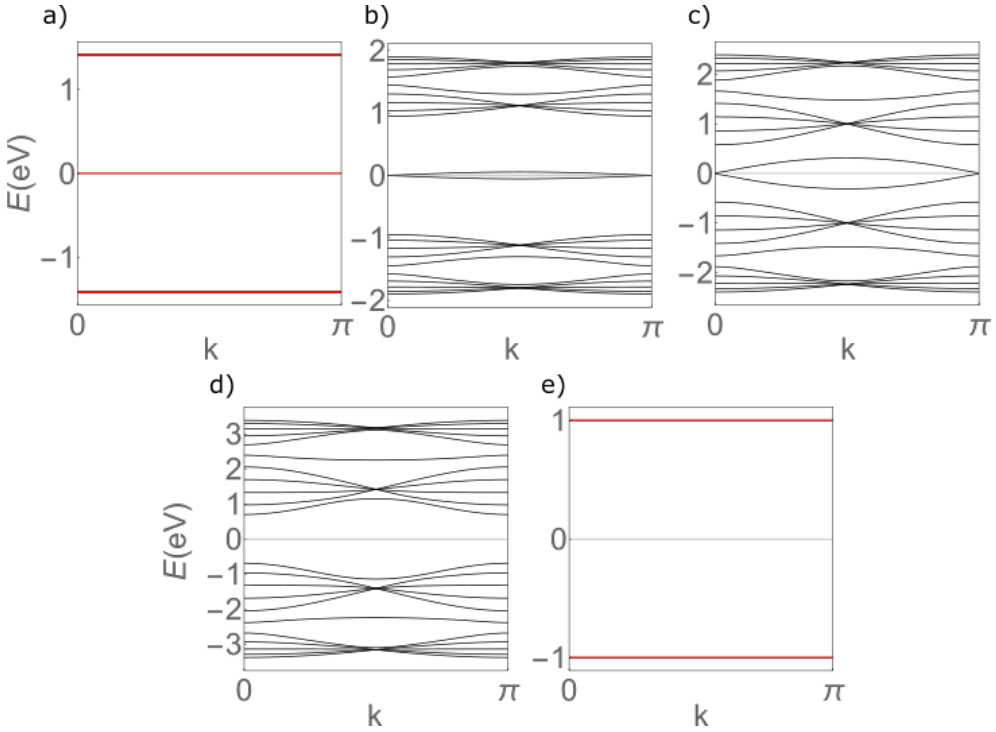

Figure 4.8: The eigenvalues $E(k)$ of a B-TGNR with flux, plotted as a function of k for $t_1 = 1$ and a) $t_2 = 0$, b) $t_2 = 0.5t_1$, c) $t_2 = t_1$, and d) $t_2 = 2t_1$. e) The eigenvalues plotted for $t_1 = 0$ and $t_2 = 1$. A gap opens up at $t_2 = t_1$.

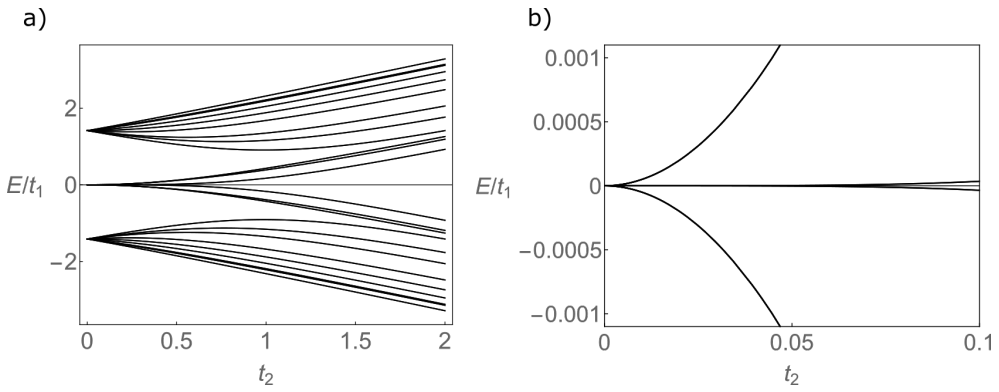

Figure 4.9: The energy spectrum of a finite system of T-graphene with bearded edges and a flux of π, plotted for a) $t_1 = 1$ and t_2 varying from 0 to $2t_1$. b) is a zoomed-in version of a).

Fig. 4.9b) showing a zoomed-in version. The zero-energy edge modes move away from zero directly upon increasing t_2. This suggests that a finite system of T-graphene with bearded edges does not become topological with a flux of π running through the square plaquettes.

In this chapter, we tried to induce a topological phase in T-graphene by introducing a flux, which would move the zero-energy excitations in the bulk away from zero, such that the edge modes at zero energy could not hybridize. However, the hybridization with the other zero-energy edge modes was not taken into account. To verify whether this is preventing the emergence of a topological phase in T-graphene, the upper and lower bearded edges were removed, as shown in Fig. 4.10a). In Fig. 4.10b), the energy spectrum of this system is shown. For $t_2 \ll t_1$ and $N > 3$, there are six bands at zero, corresponding to the six edge atoms. Upon increasing t_2, four bands move away from zero, while the other two bands stay at zero. The localization of the latter two bands is shown in Fig. 4.10c) for $t_1 = 1$ and $t_2 = 0.5$. Despite the fact that these modes are at zero energy, there is still hybridization of the edge states. There is a very small localization of the wave function on the opposite edge atoms, so the wave function does penetrate into the bulk and along the upper and lower edges.

In the next chapter, we study the electronic and topological properties of a chain of T-graphene. In this one-dimensional case, the hybridization could only occur between the two edge atoms. However, when the coupling is weak enough, we might observe a topological phase, similar to what happens in the SSH-chain.

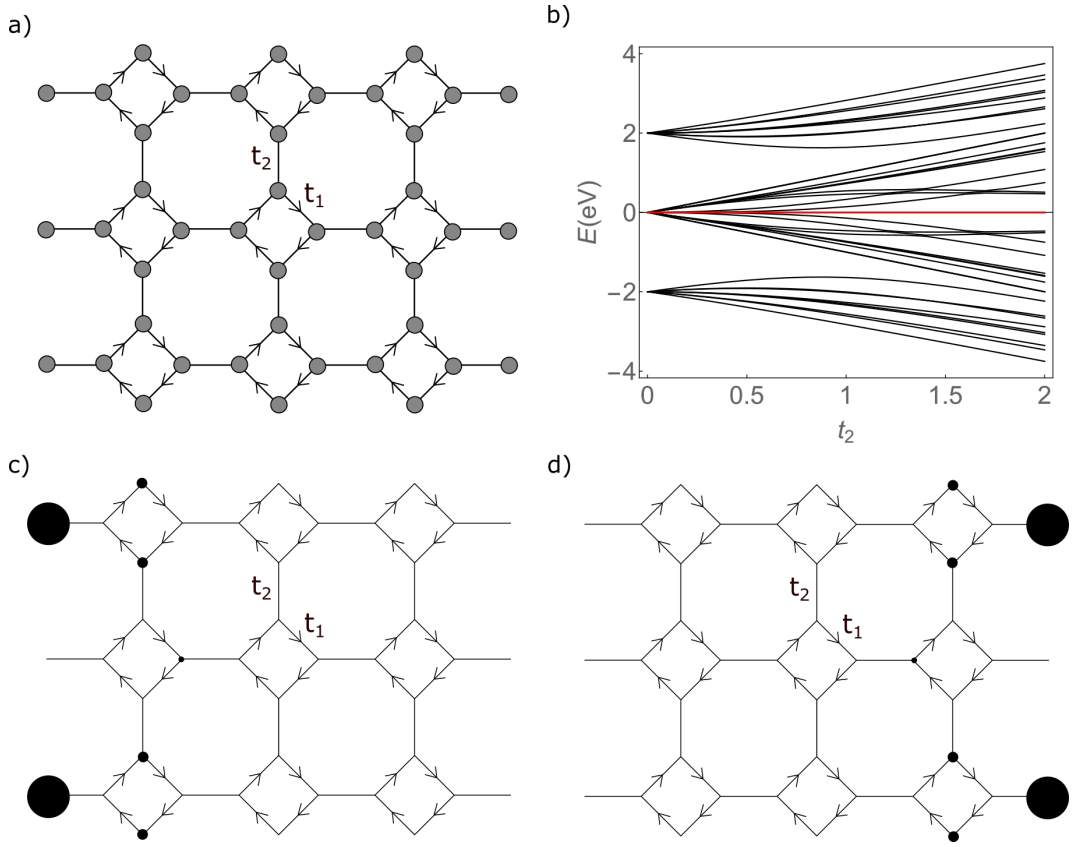

Figure 4.10: a) The structure of a finite system of T-graphene with two bearded edges, with the energy spectrum shown in b). c-d) The localization of wave functions ψ associated with c) the left zero-energy edge mode, and d) the right zero-energy edge mode. for $t_1 = 1$ and $t_2 = 0.5$. The area of the disk is proportional to $|\psi|^2$.

CHAPTER 5

A T-graphene chain in a magnetic field

In this chapter, we study a one-dimensional T-graphene chain within a magnetic field. We first introduce a homogeneous flux into a periodic chain and calculate the band structure. Next, the energy spectrum of and localization of the wave functions in a finite chain with bearded edges and flux are studied. We investigate whether the bearded edges are necessary for the localization of the wave functions by studying a finite chain without bearded edges. Lastly, we introduce a new topological invariant, the Zak phase, and calculate it for a T-graphene chain.

5.1 A periodic T-graphene chain with homogeneous flux

We consider a T-graphene chain with periodic boundary conditions, two hopping parameters t_1 and t_2 and four atoms per unit cell. A magnetic field is applied, which gives rise to a magnetic flux of Φ running through the squares. The geometric structure is shown in Fig. 5.1a). A similar structure is the rhombic or diamond chain, shown in Fig. 5.1b).

A T-graphene chain with homogeneous magnetic flux is described by the Hamiltonian

$$H_{chain} = \begin{pmatrix} 0 & -t_1 e^{i\Phi/4} & -t_2 e^{-ik} & -t_1 e^{-i\Phi/4} \\ -t_1 e^{-i\Phi/4} & 0 & -t_1 e^{i\Phi/4} & -0 \\ -t_2 e^{ik} & -t_1 e^{-i\Phi/4} & 0 & -t_1 e^{i\Phi/4} \\ -t_1 e^{i\Phi/4} & 0 & -t_1 e^{-i\Phi/4} & 0 \end{pmatrix}. \tag{5.1}$$

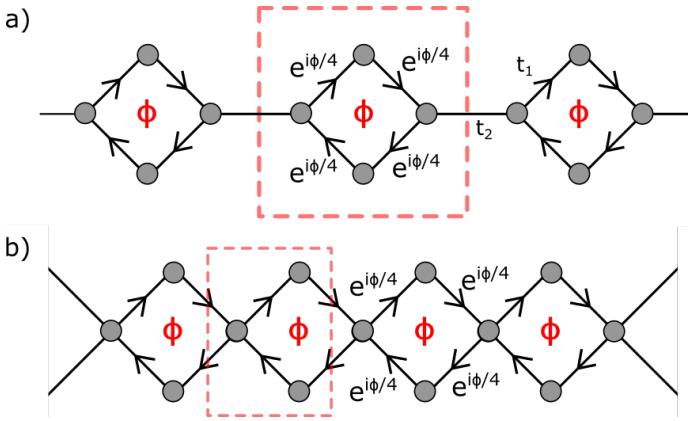

Figure 5.1: The structures of a) a periodic T-graphene chain with a magnetic flux Φ and b) a periodic rhombic chain with a magnetic flux Φ. The unit cells are marked by the dashed rectangles in red.

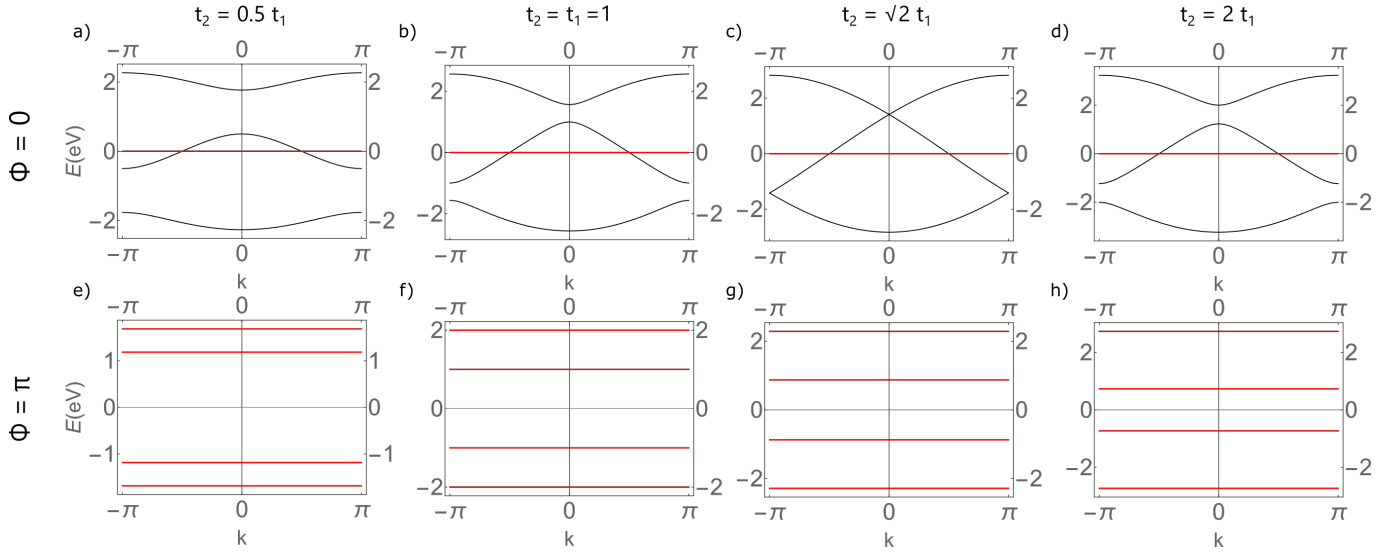

Figure 5.2: The band structures of a periodic T-graphene chain a-d) without a flux and e-h) with a π-flux, for $t_1 = 1$ and a,e) $t_2 = 0.5$, b,f) $t_2 = 1$, c,g) $t_2 = \sqrt{2}$, and d,h) $t_2 = 2$.

Similarly to the case of a two-dimensional T-graphene lattice with homogeneous flux, the hopping parameter t_1 is multiplied with a phase factor $e^{i\Phi/4}$ when moving clockwise around the square loop. The band structure was calculated for different values of t_1, t_2, and Φ, and is shown in Fig. 5.2. In the case of zero flux, there is one flat band at zero energy, independent of the value of t_2. The gap closes at three points for $t_2 = \sqrt{2}$, where band-inversions takes place. The gap opens again when t_2 is increased further. For $\Phi = \pi$, there are four flat bands at finite energy. The gap only closes at $t_1 = 0$ (or $t_2 \to \infty$). This indicates that the wave functions are localized for every value of t_1 and t_2, except for $t_1 = 0$ or $t_2 \to \infty$, when the flux $\Phi = \pi$. To further study the localization, we will consider a finite T-graphene chain with flux in the next section. For $\Phi = 2\pi$ (not shown here), the band structures are similar to those at zero flux, except the energy bands are now reflected in the k-axis. The band structures are therefore not 2π-periodic. On the other hand, the band structures for $\Phi = 4\pi$ (not shown here) are equal to those at zero flux, so they are 4π-periodic. This is similar to what we have seen for a two-dimensional T-graphene lattice with flux.

5.2 A finite T-graphene chain with bearded edges and flux

The energy spectrum calculated for a finite system with bearded edges without and with a homogeneous flux is shown in Fig. 5.3. For $\Phi = 0$, there are multiple zero-energy bands present that stay at zero when t_2 is increased from 0 to 2, with $t_1 = 1$. When including a π-flux, the zero-energy excitations in the bulk move to nonzero energies, while two edge modes stay at zero energy. Interestingly, the gap does not close for finite values of t_2. Only when $t_2 \to \infty$ (or $t_1 = 0$), the gap closes. The energy spectrum is 2π-periodic, as can be seen in Fig. 5.3. This is similar to what we found in Chapter 4 for a finite T-graphene lattice with bearded edges and flux. In the next section, we determine why the edge modes stay at zero energy for large t_2, by studying the localization of the wave functions belonging to these zero-energy edge states.

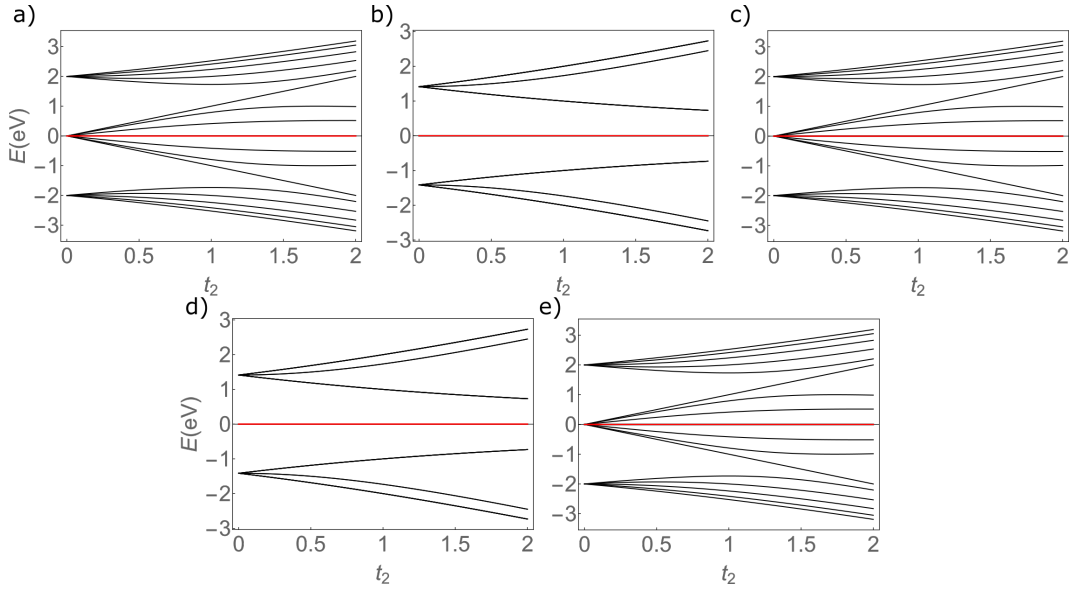

Figure 5.3: The energy spectrum of a finite-size T-graphene chain with bearded edges with $t_1 = 1$ and $N = 5$, for a) $\Phi = 0$, b) $\Phi = \pi$, c) $\Phi = 2\pi$, d) $\Phi = 3\pi$, and e) $\Phi = 4\pi$. The energy spectrum is 2π-periodic.

5.3 Localization of the wave functions

In this section, the localization of the wave functions associated with the energy bands at zero energy is calculated as a function of t_2 with $t_1 = 1$. For $t_2 < 2$, as shown in Fig. 5.4a), one of the wave functions is localized predominantly on the first edge atom and to a lesser extent on the atoms at the upper and lower corners of the first diamond in the chain. At $t_2 = 2$, the wave function is equally localized on all three atoms at the left end of the chain. For $t_2 > 2$, the wave function is predominantly localized on the two corners of the first diamond and less on the first edge atom. The other wave function shows the same localization on the right end of the chain (see Fig. 5.4b)). Interestingly, the wave functions do not penetrate into the bulk upon increasing t_2 to even higher values. This nondispersive property could explain why the edge modes stay at zero energy for every value of t_2.

A similar situation was observed experimentally for a magnetic flux in ultrafast laser-fabricated waveguide arrays in a rhombic geometry (shown in Fig. 5.1b)) [41]. In the caging limit, which is reached when a flux $\Phi = \pi$ runs through each diamond, the energy bands become nondispersive. The photons exhibit complete localization due to destructive interference of the wave functions. This type of localization is called Aharonov-Bohm (AB) caging. In our case, we observe complete localization for every nonzero value of Φ, not just for $\Phi = \pi$. Therefore, it is more accurate to use the general term *compact localized states*, which are excitations that vanish outside a finite subpart of the system (due to destructive interference of the wave functions) [42–44]. This is different from the other type of localization that we have seen, which is the protection of a topological edge state due to a symmetry of the bulk. It also differs from Anderson localization, which is caused by the absence of diffusion in a disordered medium [45].

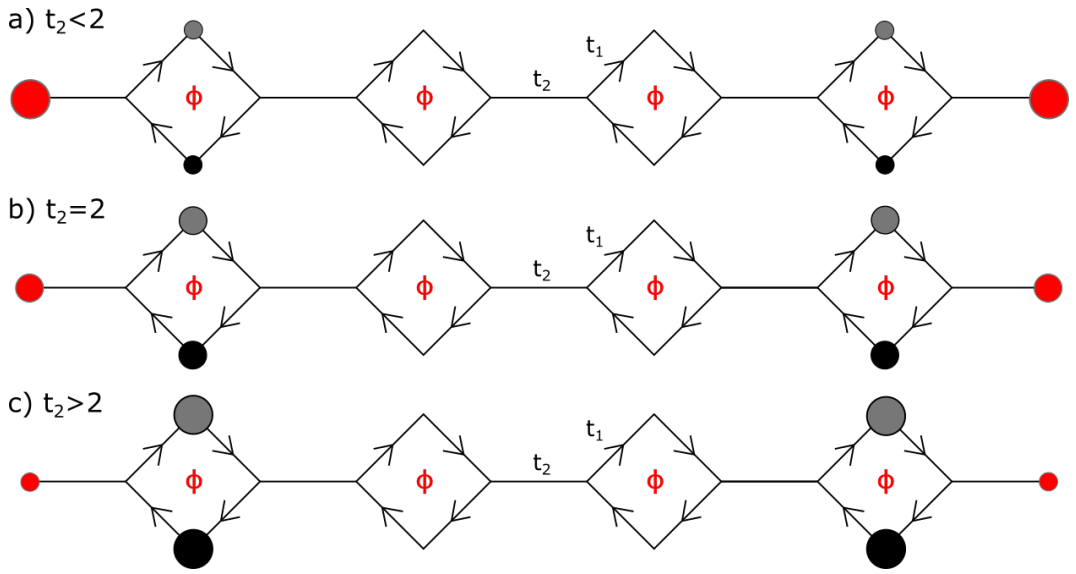

Figure 5.4: The localization of the wave functions corresponding to the flat bands at zero energy in the band structure of a finite T-graphene chain with bearded edges, for $t_1 = 1$ and a) $t_2 < 2$, b) $t_2 = 2$, and c) $t_2 > 2$. We observe compact localized states, which only delocalize at $t_1 = 0$.

5.4 A finite T-graphene chain without bearded edges

To investigate whether this localization also arises without the bearded edges, we consider a one-dimensional finite-size T-graphene chain without bearded edges and apply a magnetic field such that the flux through the squares is $\Phi = \pi$. The energy spectrum as a function of t_2 is shown in Fig. 5.5a). Interestingly, there are flat bands at nonzero energy for $\Phi = \pi$.

The localization of the wave functions corresponding to these flat bands is shown in Fig. 5.5b) for $t_1 = 1$ and $\Phi = \pi$. The wave functions are localized at the edges, where $|\psi^2|$ is twice as large at the outermost edge atoms compared to the atoms at the top and bottom of the outmost diamonds. Contrary to what we observed for the T-graphene chain with bearded edges, the localization does not change when t_2 is varied. Therefore, this system does not allow for any modification of the localization as a function of the hopping parameters.

5.5 The Zak phase of a T-graphene chain

5.5.1 The Zak phase as topological invariant

In Chapter 2, we have seen the winding number as a topological invariant to describe one-dimensional systems. Another topological invariant that is often used for one-dimensional systems is the Zak phase [46]. In the case of a T-graphene chain with magnetic flux, the Zak phase is more useful, because it is defined as the integration of the Berry connection over the one-dimensional Brillouin zone

$$\mathcal{Z}_n = \mathrm{Im} \oint dk \, \langle \psi_n(k) | \partial_k \psi_n(k) \rangle \,, \tag{5.2}$$

where $\mathcal{Z}_n$ is the Zak phase characterising the topology of the nth band and $|\psi_n(k)\rangle$ is the wave function belonging to the nth band. Typically, this integral is calculated by discretizing the path along the Brillouin zone into k_j steps with $j = 1, \ldots, N$ and $k_{N+1} =$

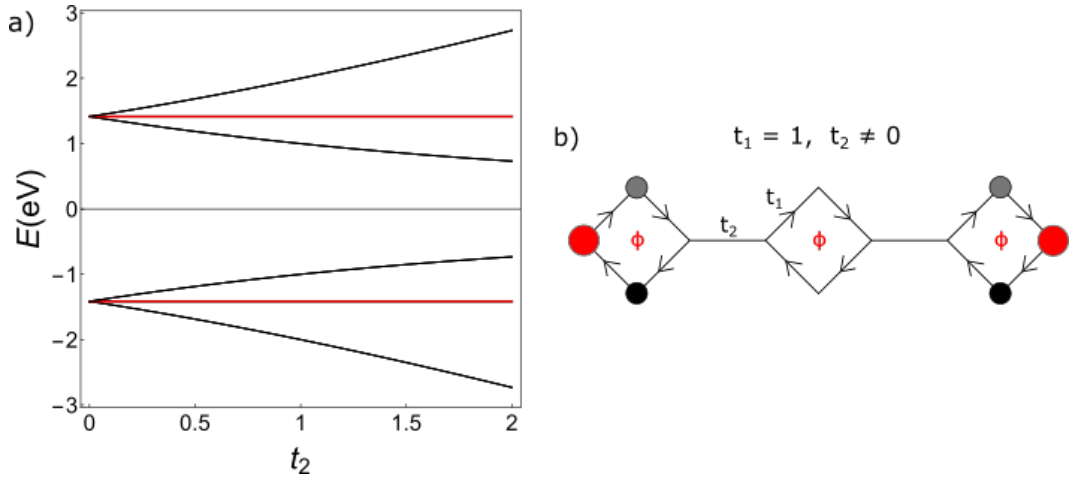

Figure 5.5: a) The energy spectrum of a T-graphene chain without bearded edges with $t_1 = 1$, $N = 5$, and $\Phi = \pi$. b) The localization of the wave functions corresponding to the flat bands for $t_1 = 1$, $t_2 \neq 0$, $N = 5$ and $\Phi = \pi$.

k_1. The integral can then be transformed into a sum as

$$\int \langle \psi_n(k) | \partial_k \psi_n(k) \rangle \, dk \to \sum_{k_j} \langle \psi_{n,k} | \partial_k \psi_{n,k} \rangle \, |_{k=k_j} \Delta k. \tag{5.3}$$

This sum can be simplified by making use of

$$\begin{aligned} \psi_{n,k+\Delta k} &\approx \psi_{n,k} + \partial_k \psi_{n,k} \Delta k; \\ \langle \psi_{n,k} | \psi_{n,k+\Delta k} \rangle &\approx 1 + \langle \psi_{n,k} | \partial_k \psi_{n,k} \rangle \, \Delta k; \\ \log \left(\langle \psi_{n,k} | \psi_{n,k+\Delta k} \rangle \right) &\approx \log \left[1 + \langle \psi_{n,k} | \partial_k \psi_{n,k} \rangle \, \Delta k \right] \approx \langle \psi_{n,k} | \partial_k \psi_{n,k} \rangle \, \Delta k. \end{aligned} \tag{5.4}$$

This yields

$$\mathcal{Z}_n = \mathrm{Im} \sum_{k_j} \log \left(\langle \psi_{n,k} | \psi_{n,k+\Delta k} \rangle \right) |_{k=k_j}. \tag{5.5}$$

We can now rewrite the sum as a sum from $j = 1$ to N, instead of a sum over all k_j, such that we can move the sum into the logarithm as a product. After choosing a step size of $\Delta k = 1$, we find

$$\begin{aligned} \mathcal{Z}_n &= \mathrm{Im} \sum_{j=1}^{N} \log \left(\left\langle \psi_{n,k_j} \middle| \psi_{n,k_j+\Delta k} \right\rangle \right); \\ &= \mathrm{Im} \log \prod_{j=1}^{N} \left\langle \psi_{n,k_j} \middle| \psi_{n,k_j+\Delta k} \right\rangle; \\ &= \mathrm{Im} \log \prod_{j=1}^{N} \left\langle \psi_{n,k_j} \middle| \psi_{n,k_{j+1}} \right\rangle. \end{aligned} \tag{5.6}$$

Physically, this is the product of N small rotations of the eigenvector's phase when it is transported along the path. The phase is then picked out by taking the imaginary part of the logarithm of the product.

5.5.2 Calculating the Zak phase of a T-graphene chain

We calculated the Zak-phase for a T-graphene chain with a homogeneous and inhomogeneous flux using Eq. (5.6). Due to the bulk-edge correspondence, we can predict the topology of the edges by calculating the Zak phase from a periodic lattice.

In Fig. 5.6, a phase diagram of the Zak phase is shown as a function of t_1/t_2 and Φ. The Zak phase is zero when t_1/t_2 is small (< 0.7) and when Φ is close to π ($2.4 < \Phi < 3.9$). It is equal to π for larger t_1/t_2 and for Φ much smaller or larger than π. The phase diagrams of the second and third band have two other regions where the Zak phase is π, namely when $t_1/t_2 = 0$ or when $\Phi = 0$. When the value of t_1/t_2 or Φ moves away from zero, the Zak phase changes to zero immediately. This was expected, because the gap is only closed for $t_1/t_2 = 0$ or $\Phi = 0$. From this analysis, it seems that the zero-modes are not protected, since there is no gap closing around zero. The Zak-phase also suggest that these modes are not protected. Further investigations are in order.

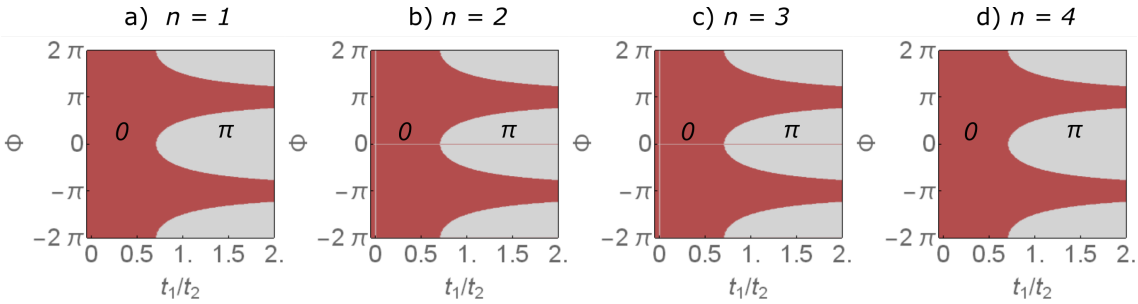

Figure 5.6: Phase diagrams of the Zak phase of the four energy bands (labeled with n) of a one-dimensional T-graphene chain, where red indicates $\mathcal{Z}_n = 0$ and gray indicates $\mathcal{Z}_n = \pi$. Notice the lines in b) and c) at $\Phi = 0$ and $t_1/t_2 = 0$.

Conclusions and outlook

In Chapter 1, we started with an introduction to the topic of electronic lattices by studying the electronic properties of graphene. Many of the special properties of graphene can be attributed to the existence of Dirac cones in the band structure. Due to the linear dispersion at these Dirac points, the density of states is zero at the Fermi energy. The linear dispersion at the Fermi-energy makes electrons behave as massless Dirac fermions, resulting in extremely high mobility of the electrons. Next, the electronic properties of graphene nanoribbons were calculated for different edge shapes, including the armchair and zigzag edges. After the discovery of graphene, other lattices were created and studied, in order to find similar or new properties, including T-graphene (or the square-octagon lattice). In Chapter 3, 4, and 5, the electronic and topological properties of different structures with a square-octagon geometry were calculated and studied. The concepts of topology, lattice symmetries, gauge fields and Berry phases were introduced in Chapter 2. Additionally, the SSH model was studied as a simple example of a topological system.

In Chapter 3, the electronic and topological properties of T-graphene were studied for different values of the intracell hopping parameter t_1 and intercell hopping parameter t_2. The dispersion relation of T-graphene showed linearity in the k_x- and k_y-directions. Furthermore, we included strain on the lattice by varying the hopping parameters independently in different directions. The band structures contained band crossings similar to critically tilted Dirac cones, as investigated in Ref. [30]. Upon changing the hopping parameters, these Dirac cones merge and a gap opens. Next, T-GNRs with different edge shapes were studied, including even armchair, odd armchair, zigzag and bearded edges. The band structure of A-TGNRs showed Dirac cones, with the number of Dirac cones increasing with the width of the nanoribbon. For B-TGNRs, the band structure contained flat bands at finite energy, which indicate the presence of localized wave functions. This was studied further in a finite T-graphene lattice with bearded edges. However, the zero-energy bands in the energy spectrum moved away from zero energy immediately when the hopping t_2 between the edge and the bulk was increased to slightly above zero. The immediate delocalization of the wave functions belonging to the edge modes suggests the absence of a topological phase, due to the hybridization of the zero-energy edge states with the zero-energy excitations in the bulk.

A magnetic field was introduced in Chapter 4 to open the gap of bulk T-graphene to prevent the above mentioned hybridization. We studied two types of flux, homogeneous and inhomogeneous, and found that they are different, despite the fact that, in both cases, a phase Φ is picked up when moving around the square loop. We verified that the gap of bulk T-graphene could be opened by introducing a π-flux into a finite system without bearded edges. Next, we calculated the energy spectrum of a finite system with bearded edges and flux. We expected robust zero-energy edge modes, but found instead that the edge modes moved away from zero energy directly upon increasing t_2, despite the introduction of a magnetic flux. By studying the localization, we discovered that the edge states also hybridize with the other zero-energy edge states.

In Chapter 5, a one-dimensional chain with a flux π was investigated. In this system, the edge states can only hybridize with the edge state at the other side of the chain. We expected to see some localization for small values of the hopping between the edges and the bulk. The band structure of a periodic T-graphene chain contained flat bands at non-zero energy for $\Phi = \pi$. Additionally, the energy spectrum of a finite chain with bearded edges showed flat bands at zero-energy, but the gap did not close for $t_2 \neq 0$. Upon looking at the localization, we found compact localized states. The zero-energy wave functions were localized at the edge or at the upper and lower corners of the first and last diamond in the chain, and do not penetrate into the bulk. This localization was also observed for a finite T-graphene chain without bearded edges. However, these localized states had a nonzero energy. Lastly, the Zak phase of a T-graphene chain was calculated. The phase diagrams clearly showed that the Zak phase changes immediately from π to 0 upon increasing Φ or t_1/t_2 from zero to slightly above zero.

We can conclude that T-graphene (in both one- and two-dimensional structures) does not exhibit any topological property with the flux as introduced in Chapter 4. Nevertheless, the compact localized states found in a finite T-graphene chain with bearded edges have the same robust property as topologically protected edge states. One can ask whether compact localized states can be called topological because of the strong localization exhibited by the wave functions at the edges. However, when the Zak phase changes from 0 to π, the system undergoes a quantum phase transition from a critical phase to another phase. We cannot straightforwardly call this other phase topological because there is no trivial phase. It is possible that the definition of the Zak phase is not sufficient to describe the phase transition in a T-graphene chain. Further research is needed to investigate the compact localized states and the phase transition more closely.

Furthermore, we focused on using a magnetic field to open the gap throughout this thesis. However, there exist other ways to open the gap in the T-graphene chain in order to obtain compact localized states. One possibility is introducing superconductivity into the chain, which is similar to the Kitaev chain [47]. Systems with superconductivity show particle-hole symmetry, which is discussed in section 2.1.3. The superconducting energy gap is a consequence of the energy that is gained when two electrons form a Cooper pair. Another way of opening the gap is Rashba coupling [48], which is a direct result of inversion symmetry breaking.

Another opportunity can be found in the experimental realization of an electronic T-graphene lattice [49] with a flux. However, there are some practical complications. A magnetic field of $4T$ corresponds to a flux $\Phi = 2 \cdot 10^{-3}\Phi_0$. This is too small to observe possible compact localized states, even though only a small flux is necessary. However, a one-dimensional photonic lattice with square-octagon geometry can be realized, similar to the waveguide arrays in a rhombic geometry mentioned in Chapter 5. The experimental results could be used to confirm our theoretical predictions and further study the properties of the T-graphene chain.

Bibliography

[1] K. S. Novoselov, A. K. Geim, S. V. Morozov, D. Jiang, Y. Zhang, S. V. Dubonos, I. V. Grigorieva, and A. A. Firsov. Electric Field Effect in Atomically Thin Carbon Films. *Science*, **306**(5696): 666–669, 2004.

[2] S. M. Choi, S. H. Jhi, and Y. W. Son. Effects of strain on electronic properties of graphene. *Physical Review B*, **81**: 081407, 2010.

[3] G. van Miert, C. Morais Smith, and V. Juričić. High-Chern-number bands and tunable Dirac cones in β-graphyne. *Physical Review B*, **90**(8): 081406, 2014.

[4] G. van Miert, V. Juričić, and C. Morais Smith. Tight-binding theory of spin-orbit coupling in graphynes. *Physical Review B*, **90**: 195414, 2014.

[5] D. Malko, C. Neiss, and A. Görling. Two-dimensional materials with Dirac cones: Graphynes containing heteroatoms. *Physical Review B*, **86**(4): 045443, 2012.

[6] D. Malko, C. Neiss, F. Vines, and A. Görling. Competition for graphene: graphynes with direction-dependent Dirac cones. *Physical Review Letters*, **108**(8): 086804, 2012.

[7] Y. Liu, G. Wang, Q. Huang, L. Guo, and X. Chen. Structural and electronic properties of T graphene: a two-dimensional carbon allotrope with tetrarings. *Physical Review Letters*, **108**(22): 225505, 2012.

[8] F. D. M. Haldane. Model for a quantum Hall effect without Landau levels: Condensed-matter realization of the" parity anomaly". *Physical Review Letters*, **61**(18): 2015, 1988.

[9] C. L. Kane and E. J. Mele. Quantum spin Hall effect in graphene. *Physical Review Letters*, **95**(22): 226801, 2005.

[10] C. L. Kane and E. J. Mele. Z_2 Topological Order and the Quantum Spin Hall effect. *Physical Review Letters*, **95**(14): 146802, 2005.

[11] B. A. Bernevig, T. L. Hughes, and S. C. Zhang. Quantum spin Hall effect and topological phase transition in HgTe quantum wells. *Science*, **314**(5806): 1757–1761, 2006.

[12] M. Franz and L. Molenkamp. Topological Insulators. Vol. 6. Elsevier, 2013.

[13] W. A. Harrison. Electronic structure and the properties of solids: the physics of the chemical bond. Freeman, 1980, 90.

[14] A. C. Neto, F. Guinea, N. M. Peres, K. S. Novoselov, and A. K. Geim. The electronic properties of graphene. *Reviews of Modern Physics*, **81**(1): 109–162, 2009.

[15] D. G. Papageorgiou, I. A. Kinloch, and R. J. Young. Mechanical properties of graphene and graphene-based nanocomposites. *Progress in Materials Science*, **90**: 75–127, 2017.

[16] C. Lee, X. Wei, J. W. Kysar, and J. Hone. Measurement of the elastic properties and intrinsic strength of monolayer graphene. *Science*, **321**(5887): 385–388, 2008.

[17] S. Wan, Y. Li, J. Mu, A. E. Aliev, S. Fang, N. A. Kotov, L. Jiang, Q. Cheng, and R. H. Baughman. Sequentially bridged graphene sheets with high strength, toughness, and electrical conductivity. *Proceedings of the National Academy of Sciences*, **115**(21): 5359–5364, 2018.

[18] A. Kuzmenko, E. Van Heumen, F. Carbone, and D. Van Der Marel. Universal optical conductance of graphite. *Physical Review Letters*, **100**(11): 117401, 2008.

[19] K. Wakabayashi, K. Sasaki, T. Nakanishi, and T. Enoki. Electronic states of graphene nanoribbons and analytical solutions. *Science and Technology of Advanced Materials*, **11**(5): 054504, 2010.

[20] Y. W. Son, M. L. Cohen, and S. G. Louie. Energy Gaps in Graphene Nanoribbons. *Physical Review Letters*, **97**(21): 216803, 2006.

[21] A. Maffucci and G. Miano. Transmission Line Model of Graphene Nanoribbon Interconnects. *Nanoscience and Nanotechnology Letters*, **5**(11): 1207–1216, 2013.

[22] M. Stähler. Spectrum of Electrons in Graphene Nanoribbons. Bachelor Thesis. Universität Augsburg, 2014.

[23] X. Bi, J. Jung, and Z. Qiao. Role of geometry and topological defects in the one-dimensional zero-line modes of graphene. *Physical Review B*, **92**(23): 235421, 2015.

[24] M. Fujita, K. Wakabayashi, K. Nakada, and K. Kusakabe. Peculiar Localized State at Zigzag Graphite Edge. *Journal of the Physical Society of Japan*, **65**(7): 1920–1923, 1996.

[25] R Peierls. Quantum Theory of Solids (Clarendon, Oxford). 1955.

[26] X. Sun, J. Li, and C. Wu. Electron Correlation and Peierls Instability. In: *Interacting Electrons in Reduced Dimensions*. Springer, 1989, 179–188.

[27] J. K. Asbóth, L. Oroszlány, and A. Pályi. A short course on topological insulators. *Lecture Notes in Physics*, **919**, 2016.

[28] K von Klitzing, G. Dorda, and M. Pepper. New method for high-accuracy determination of the fine-structure constant based on quantized Hall resistance. *Physical Review Letters*, **45**(6): 494, 1980.

[29] E. H. Hall. On a new action of the magnet on electric currents. *American Journal of Mathematics*, **2**(3): 287–292, 1879.

[30] M Milićević, G Montambaux, T Ozawa, I Sagnes, A Lemaître, L. L. Gratiet, A Harouri, J Bloch, and A Amo. Tilted and type-III Dirac cones emerging from flat bands in photonic orbital graphene. *arXiv:1807.08650*, 2018.

[31] C. Dai, X. Yan, Y Xiao, and Y. Guo. Electronic and transport properties of T-graphene nanoribbon: Symmetry-dependent multiple Dirac points, negative differential resistance and linear current-bias characteristics. *Europhysics Letters*, **107**(3): 37004, 2014.

[32] X. Q. Wang, H. D. Li, and J. T. Wang. Structural stabilities and electronic properties of planar C4 carbon sheet and nanoribbons. *Physical Chemistry Chemical Physics*, **14**(31): 11107–11111, 2012.

[33] D. Klein. Graphitic polymer strips with edge states. *Chemical Physics Letters*, **217**(3): 261–265, 1994.

[34] K. Wakabayashi, S. Okada, R. Tomita, S. Fujimoto, and Y. Natsume. Edge States and Flat Bands of Graphene Nanoribbons with Edge Modification. *Journal of the Physical Society of Japan*, **79**(3): 034706, 2010.

[35] Y. Plotnik, M. C. Rechtsman, D. Song, M. Heinrich, J. M. Zeuner, S. Nolte, Y. Lumer, N. Malkova, J. Xu, A. Szameit, et al. Observation of unconventional edge states in 'photonic graphene'. *Nature Materials*, **13**(1): 57, 2014.

[36] S. Freeney, J. van den Broeke, A. van der Veen, I Swart, and C Morais Smith. Edge-dependent topology in Kekulé lattices. *arXiv:1906.09051*, 2019.

[37] H. Min, J. Hill, N. A. Sinitsyn, B. Sahu, L. Kleinman, and A. H. MacDonald. Intrinsic and Rashba spin-orbit interactions in graphene sheets. *Physical Review B*, **74**(16): 165310, 2006.

[38] Y. A. Bychkov and E. I. Rashba. Properties of a 2D electron gas with lifted spectral degeneracy. *JETP Letters*, **39**(2): 78, 1984.

[39] R. Peierls. Zur theorie des diamagnetismus von leitungselektronen. *Zeitschrift für Physik*, **80**(11-12): 763–791, 1933.

[40] D. R. Hofstadter. Energy levels and wave functions of Bloch electrons in rational and irrational magnetic fields. *Physical Review B*, **14**(6): 2239, 1976.

[41] S. Mukherjee, M. Di Liberto, P. Öhberg, R. R. Thomson, and N. Goldman. Experimental observation of Aharonov-Bohm cages in photonic lattices. *Physical Review Letters*, **121**(7): 075502, 2018.

[42] M. Röntgen, C. V. Morfonios, and P. Schmelcher. Compact localized states and flat bands from local symmetry partitioning. *Physical Review B*, **97**: 035161, 2018.

[43] W. Maimaiti, A. Andreanov, H. C. Park, O. Gendelman, and S. Flach. Compact localized states and flat-band generators in one dimension. *Physical Review B*, **95**: 115135, 2017.

[44] M. Röntgen, C. V. Morfonios, I. Brouzos, F. K. Diakonos, and P. Schmelcher. Quantum Network Transfer and Storage with Compact Localized States Induced by Local Symmetries. *Physical Review Letters*, **123**: 080504, 2019.

[45] P. W. Anderson. Absence of diffusion in certain random lattices. *Physical Review*, **109**(5): 1492, 1958.

[46] P. Delplace, D Ullmo, and G Montambaux. Zak phase and the existence of edge states in graphene. *Physical Review B*, **84**(19): 195452, 2011.

[47] M. Greiter, V. Schnells, and R. Thomale. The 1D Ising model and the topological phase of the Kitaev chain. *Annals of Physics*, **351**: 1026–1033, 2014.

[48] B. Braunecker, G. I. Japaridze, J. Klinovaja, and D. Loss. Spin-selective Peierls transition in interacting one-dimensional conductors with spin-orbit interaction. *Physical Review B*, **82**(4): 045127, 2010.

[49] M. R. Slot, T. S. Gardenier, P. H. Jacobse, G. C. van Miert, S. N. Kempkes, S. J. Zevenhuizen, C. M. Smith, D. Vanmaekelbergh, and I. Swart. Experimental realization and characterization of an electronic Lieb lattice. *Nature Physics*, **13**(7): 672, 2017.